Department of Physics and Astronomy
Heidelberg University

Master Thesis in Physics
submitted by
Isabel Sainz Saenz-Diez
born in Santiago de Compostela, Spain

2024

First study of the $W\gamma\gamma$ production in pp collisions at $\sqrt{s} = 13.6\,\text{TeV}$ with the ATLAS detector

This Master Thesis has been carried out by
Isabel Sainz Saenz-Diez
at the Kirchhof Institute for Physics
under the supervision of
Prof. Dr. Hans-Christian Schultz-Coulon

Zusammenfassung

Präzisionsmessungen von Prozessen, an denen mehrere elektroschwache Eichbosonen beteiligt sind, sind ein hervorragender Test der Eichstruktur des Standardmodells und eine potenzielle Quelle für neue Physik. In dieser Arbeit wird der $W\gamma\gamma$-Produktionsprozess, bei dem das W-Boson leptonisch zerfällt, im laufenden Run 3 des LHC bei einer Schwerpunktsenergie von $\sqrt{s} = 13,6\,\text{TeV}$ untersucht. Die vom ATLAS-Detektor in den ersten beiden Jahren von Run 3 aufgezeichneten Daten werden analysiert, was einer integrierten Luminosität von $L_{int} = 59\,\text{fb}^{-1}$ entspricht. Die für Run 3 eingeführten Verbesserungen am Triggersystem werden für den besonderen Fall der $l\gamma\gamma$-Triggerketten untersucht, wobei sich eine gute Übereinstimmung bei den Effizienzen zeigt. Bei der $W\gamma\gamma$-Analyse werden verschiedene Signaldatensätze verglichen und die Schätzung von Signal und Untergrund durch MC-Simulationen vorgestellt. Zusätzlich werden die Ergebnisse mit der Messung des $W\gamma\gamma$-Prozesses verglichen, die von ATLAS für Run 2 bei $\sqrt{s} = 13\,\text{TeV}$ durchgeführt wurde. Die Anzahl der erwarteten Ereignisse für Run 3 ist um 4% höher als in Run 2. Diese Zuhname ist aufgrund der höheren Schwerpunktsenergie zu erwarten und zeigt eine gute Übereinstimmung zwischen den beiden Messungen.

Abstract

Precision measurements of processes involving multiple electroweak gauge bosons are an excellent probe of the gauge structure of the Standard Model and a potential source of new physics. In this thesis, the $W\gamma\gamma$ production process, with the W boson decaying leptonically, is studied in the ongoing Run 3 of the LHC at a centre-of-mass energy of $\sqrt{s} = 13.6\,\text{TeV}$. The data recorded by the ATLAS detector the first two years of Run 3 is analysed, which corresponds to an integrated luminosity of $L_{int} = 59\,\text{fb}^{-1}$. The upgrades introduced on the trigger system for Run 3 are studied for the particular case of the $l\gamma\gamma$ trigger chains, showing good agreement in the efficiencies. In the $W\gamma\gamma$ analysis, different signal samples are compared and the estimation of signal and backgrounds through MC simulations is presented. Additionally, the results are compared to the measurement of the $W\gamma\gamma$ process performed by ATLAS for Run 2 at $\sqrt{s} = 13\,\text{TeV}$. The number of expected events for Run 3 is 4% higher than in Run 2. This increase is expected due to the higher centre-of-mass energy and shows good agreement between the two measurements.

Contents

1 Introduction **3**

2 Theoretical background **5**

2.1 The Standard Model of Particle Physics 5

2.2 Electroweak Interactions 7

2.3 Triple Gauge Boson Processes 8

3 The ATLAS Experiment at the LHC **11**

3.1 The Large Hadron Collider 11

3.2 The ATLAS Experiment 12

4 Particle Reconstruction and Monte Carlo Simulations **19**

4.1 Particle Reconstruction Algorithms 19

4.2 Monte Carlo Simulations 23

4.3 Framework and Analysis Formats 24

5 Data and Monte Carlo Samples **27**

6 Trigger Performance Studies **29**

6.1 Trigger Chains 29

6.2 Trigger Analysis Strategy 31

6.3 Object and Event Selection 32

6.4 Trigger Performance 37

6.5 Trigger Matching Efficiencies 40

7 $W\gamma\gamma$ Analysis **43**

7.1 Signal and Background Processes 43

7.2 Object and Event Selection 46

7.3 Signal Estimation and Sample Comparison 49

7.4 Background Estimation 56

7.5 Results 59

8 Summary **63**

A Trigger Performance Studies Distributions for the Muon Channel **65**

B Signal Electron Channel MC Sample Validation **66**

C Signal Electron Channel MC Results **67**

D Signal Muon Channel MC Results **68**

E Missing Transverse Energy Resolution **69**

1 Introduction

In the past decades, the field of particle physics has reached a climax with the discovery of the Higgs boson in 2012. This brought a major success to the Large Hadron Collider (LHC) and the European Organisation for Nuclear Research (CERN), which saw one of its main goals being achieved. The confirmation of how the elementary particles acquire their mass was a milestone for the Standard Model of Particle Physics (SM).

However, it did not stop with the Higgs boson. Ever since then, the SM has been under close scrutiny in the search of any deviation that could lead to the answer of the remaining open questions, such as the matter-antimatter asymmetry in the universe, the mechanism through which neutrinos acquire their mass or the nature of dark matter (DM). For the latter, several candidates have been proposed in beyond the Standard Model (BSM) scenarios, to which the LHC has placed strong bounds via direct and indirect searches [1].

The different experiments within the LHC do not only seek for the discovery of new particles, but also keep on testing the SM predictions. The increasing precision in the measurements opens the door to potential anomalies that could give hints of new physics phenomena. This is the case for the electroweak gauge bosons self-interactions, which are indeed predicted by the electroweak theory of the SM. In order to study the gauge structure of this theory, several double and triple gauge boson production processes have been studied in the last years, in particular by the ATLAS and CMS experiments at the LHC. The case of processes involving three gauge bosons in the final state is particularly interesting since they are sensitive to triple and quartic gauge couplings. The measurement of these processes can be interpreted through an Effective Field Theory (EFT), which does not depend in any BSM theory and would allow to measure anomalies in these couplings.

In this thesis, the triple gauge boson production of a W boson in association with two photons is studied. The analysis is based on the data recorded by the ATLAS experiment in the ongoing data-taking period, Run 3. This process has recently been observed based on Run 2 data [2], but the ATLAS experiment has undergone several upgrades in between that will enhance the observation of this process and will be more sensitive to potential anomalies. In the upcoming years, the LHC will enter the High Luminosity era (HL-LHC) that comes with numerous experimental upgrades and will extend the current accessible data. Adapting to these upgrades and comparing new high precision measurements with previous observations is a constant challenge.

The scope of this thesis provides a first glance into the $W\gamma\gamma$ process in Run 3, as well as the validation of relevant upgrades in the ATLAS detector. The structure is the following. In Chapter 2, an overview of the theoretical background with an introduction to the SM is given. The focus of this chapter lies on the electroweak sector of the theory and the triple gauge boson processes that have been measured with the ATLAS experiment. In Chapter 3, the Large Hadron Collider and, in particular, the ATLAS detector are described, with special attention to the trigger system and its upgrades for Run 3. The explanation of the particle reconstruction algorithms in ATLAS, as well as the basis of Monte Carlo (MC) Simulations in particle physics and the introduction of

the ATLAS software framework are given in Chapter 4. In Chapter 5, the data and MC samples used in the thesis and their details are included. The first part of the analysis of this thesis consists of trigger performance studies relevant for the $W\gamma\gamma$ process, which are described in Chapter 6. In Chapter 7, the $W\gamma\gamma$ analysis is presented. The signal and background processes are explained, along with the definition of the signal region and its event estimation. A summary is presented in Chapter 8.

Author's Contribution

As the work in big collaborations such as ATLAS is usually the combination of different parts, the clarification of the contribution of the author to the results presented in this thesis is needed.

My contribution to the $W\gamma\gamma$ analysis mainly consists in the migration from the Run 2 to the Run 3 setup of the ATLAS experiment. I developed a framework for the $W\gamma\gamma$ analysis[1], based on the general ATLAS Athena framework. This presented significant changes with respect to Run 2, starting from the basic structure of the framework. This also involved the validation of several tools needed for the analysis that in some cases presented significant changes with respect to previous Athena versions. From all of the tools that I tested, a problem was found in one of them, and it was reported to the responsible developers of the tool.

Regarding the analysis formats used, I constructed the $W\gamma\gamma$ framework in such a way that it can not only work with old data and MC formats, but also with the lastest formats developed in ATLAS: PHYS and PHYSLITE. Just a few analysis have used these formats, but they are intended to replace the old formats in the upcoming years. All of the samples analysed were centrally produced and requested by other analysis teams in ATLAS, with the exception of one of the signal samples. This involved the local production of a sample, its validation and further discussion in ATLAS meetings, before it was centrally produced. The local production of the sample was done with the help of PhD student Thomas Junkermann.

[1]The $W\gamma\gamma$ framework can be accessed at `https://gitlab.cern.ch/issainzs/WyyAnalysis`

2 Theoretical background

The Standard Model of Particle Physics (SM) embodies the description of the fundamental constituents of ordinary matter. It includes a successful description of the electromagnetic, weak and strong interactions, based on the interplay of theory and experimental evidences [3]. However, it neither includes the fourth of the interactions, the gravitational force, nor provides a proper description of Dark Matter, which makes up to 27% of the universe, in contrast to the 5% of ordinary matter [4], among other open questions.

SM Electroweak processes have sensitivity to new physics which can hold some of the answers. Precision measurements on triple gauge boson processes and, in particular $W\gamma\gamma$, could potentially show deviations from the theory of the SM, that could indicate new physics. The way to look for it is through the Effective Field Theory (EFT) and in order to test it, the SM processes have to be well understood.

In the following section, an introduction to the SM is given, followed by a more detailed explanation of the theory within the SM that is most relevant for the process being studied in this thesis, the Electroweak Theory. The section is closed by a brief introduction to EFTs and an overview of the existing triple gauge boson analyses.

2.1 The Standard Model of Particle Physics

The SM describes the strong, weak and electromagnetic (EM) interactions between the fundamental particles in the form of a relativistic quantum field theory (QFT), based on the principle of gauge invariance [3, 5].

The classification of particles is based on the spin s, depending on whether they are fermions, with half-integer spin ($s = 1/2$), or bosons, with integer spin ($s = 0, 1$). The fundamental fermions are further divided into *leptons* and *quarks*. In the case of the leptons, the electron e, muon μ and tau τ, with their respective flavour neutrinos ν compose three families. While the neutrinos are neutral, the other leptons have charge e, where e represents the unit electron charge. On the other hand, the quarks are divided into two types and come in a total of six flavours:

- Up-type quarks of charge $Q = +2/3e$: up, charm and top
- Down-type quarks of charge $Q = -1/3e$: down, strange and bottom

The quark families are divided in three pairs of up and down-type quarks combinations in the following order: (u, d), (c, s) and (t, b).

Both lepton and quark families are in the order of increasing mass, where transitions within a family is favoured, with the exception of the neutrinos, where a normal (increasing mass) or inverted hierarchy are possible [6, 7]. In addition to these particles, every fermion has a correspondent anti-fermion with opposite charge.

The vector *gauge bosons* (bosons with spin $s = 1$) are responsible for the mediation of the SM interactions. In the case of the electromagnetic interaction, the pho-

tons γ couple to charged particles and, since they are neutral and massless gauge bosons, they do not self-interact. In the weak interaction, the $W^{\pm}$ and Z bosons are the mediators and they have a mass of 80.377 GeV and 91.187 GeV respectively. In the case of the W bosons, they enable quark flavour mixing as described in the the Cabibbo–Kobayashi–Maskawa (CKM) Matrix [8, 9], being the transitions between quarks from the same family maximal. The Z boson only participates in same-flavour quark interactions (particle-antiparticle pairs), having no preference among leptons - generally referred as *lepton universality* [10].

The last of the three interactions included in the SM is the strong force, which involves the interaction of quarks and gluons via the exchange of a new type of charge, the colour. Colour comes as red, green and blue (r, g, b) and their respective anti-colour. It was introduced as an extra degree of freedom that solved the spin-statistics problem in the original quark model proposed by M. Gell-Mann and G. Zweig [11]. Additionally, experimental evidences showed that single quarks or gluons cannot be observed, which is known as *colour confinement*, since only colourless states are observable. Quarks appear in nature only as combination in hadrons: mesons $(q\bar{q})$, baryons (qqq) or even pentaquarks $(qqqq\bar{q})$ [12]. On the contrary, gluons do not combine and cannot be observed, but self-interactions are allowed by the SM.

The only scalar boson (with spin $s = 0$) of the SM is the *Higgs Boson*, which is the responsible for giving mass to fermions and gauge bosons through the so-called Higgs Mechanism through an *spontaneous symmetry breaking* [13, 14]. It was discovered in 2012 [15, 16] at a mass of $m_H = 125.25\,\text{GeV}$.

The SM QFT

All of the information of the SM is contained in the Lagrangian $\mathcal{L}$ [17] by the combination of the descriptions of boson fields, the interactions, the Higgs field and the mass terms via Higgs interaction. It relies in the verification of the gauge principle for symmetry operations requiring the invariance of $\mathcal{L}$ under local transformations. The symmetry group of the SM is $SU(3)_c \otimes SU(2)_L \otimes U(1)_Y$ [2], where the subscripts are the generators of the symmetry and are associated with the gauge vector boson fields:

- $SU(3)_c$ is the symmetry group of Quantum Chromodynamics (QCD), describing the strong force
- $U(1)_Y$ is the symmetry group of Quantum Electrodynamics (QED), describing the EM interaction
- $SU(2)_L \otimes U(1)_Y$ is the symmetry group of the Electroweak (EW) theory, unifying the weak and EM interactions.

[2] The S denotes a special symmetry group with matrices of determinant 1, while U denotes unitary matrices, i.e. $UU^{-1} = UU^{\dagger} = \mathbb{I}$.

2.2 Electroweak Interactions

The EW Interactions are an interplay of electromagnetic and weak interactions, which can be better understood when first looking at the two forces separately. The unification of both interactions was developed by Glashow, Salam and Weinberg [18, 19, 20].

Electromagnetic Interactions

The QED lagrangian is constructed in order to preserve invariance under a local $U(1)_Y$ transformation, where the fermion Dirac field undergoes $\psi(x) \rightarrow e^{i\alpha(x)}\psi(x)$, giving rise to the EM interaction. From requiring only invariance under global transformations, some non-vanishing terms appear and the addition of the gauge vector boson fields fulfils then the invariance. This results in:

$$\mathcal{L}_{QED} = i\bar{\psi}\gamma^{\mu}\left(\partial_{\mu} + ieA_{\mu}\right)\psi - m\bar{\psi}\psi - \frac{1}{4}F_{\mu\nu}F^{\mu\nu} \tag{1}$$

with $F_{\mu\nu} = \partial_{\mu}A_{\nu} - \partial_{\nu}A_{\mu}$ as the vector tensor field and A_{μ} the vector boson field. $\mathcal{L}_{QED}$ preserves invariance under the gauge transformation with the covariant derivative $D_{\mu} = \partial_{\mu} + ieA_{\mu}$.

The Weak Force

While the EM interaction conserves charge and parity[3], in the weak interaction the combined charge-parity (CP) symmetry is maximally violated. This is evidenced by the exclusive coupling of the W boson to left-handed fermions, i.e. with negative helicity[4], and right-handed anti-fermions. These fermions are grouped in doublets, for the left-handed case, and singlets, for the right-handed case:

$$\begin{pmatrix}\nu_e \\ e^-\end{pmatrix}, \begin{pmatrix}u \\ d\end{pmatrix} \qquad \& \qquad e^-_R, u_R, d_R \tag{2}$$

where neutrinos are only part of the left-handed doublet, since there are no right-handed neutrinos. The same stands for other same family combinations and the anti-fermions. The corresponding symmetry of this interaction is the $SU(2)_L$, which applies flavour transformations on the doublets, while the right-handed ones remain unchanged. The generators of this symmetry are the Pauli matrices σ_i and a new quantum number is introduced: the *weak isospin* T. Its value is $T = 1/2$ and the its third component $T_3 = \pm 1/2$. For the right-handed ones the weak isospin is $T = T_3 = 0$.

Electroweak Unification

Unifying EM and weak interactions results in a $SU(2)_L \otimes U(1)_Y$ symmetry that preserves gauge invariance. The introduction of the *hypercharge* Y relates the weak isospin with

[3] A parity transformation changes the sign of the spatial coordinates of the particle.

[4] The helicity consists in the projection of the spin on the direction of the particle momentum

the electric charge by $Y = 2(Q - T_3)$.

The final constructed lagrangian involves covariant derivatives from three fields of the $S(2)_L$ with coupling g_W and one field from $U(1)_Y$ with coupling g', W^i_μ and B_μ respectively:

$$\mathcal{L}_{EW} = \sum_\psi \left[\bar{\psi}^L i\gamma^\mu D_\mu \psi^L + \bar{\psi}^R i\gamma^\mu D_\mu \psi^R\right] - \frac{1}{4} B_{\mu\nu} B^{\mu\nu} - \frac{1}{4}\sum_{i=1}^{3} W^i_{\mu\nu} W_i^{\mu\nu}, \tag{3}$$

where $D_\mu = \partial_\mu + ig_W \vec{W}_\mu \vec{T} + ig' B_\mu Y$ is the covariant derivative in this case, where $T = \sigma/2$.

The four fields present in the EW lagrangian, in contrast to the A_μ field in the EM lagrangian, do not correspond to the physical vector boson fields. In the case of the W boson fields, they are built as the combination of $W^\pm_\mu = \frac{1}{\sqrt{2}}\left(W^1_\mu \mp iW^2_\mu\right)$, as a result of the spontaneous symmetry breaking of the EW symmetry.

For the photon and the Z boson, noting that they interact with the same particles with the only exclusion of the neutrinos, they arise from the mixture of the other two fields, W^3_μ and B_μ, with the introduction of a mixing angle, know as the *Weinberg angle* θ_W:

$$A_\mu = B_\mu cos\theta_W + W^3_\mu sin\theta_W \quad \& \quad Z_\mu = -B_\mu sin\theta_W + W^3_\mu cos\theta_W. \tag{4}$$

The Weinberg angle also relates the coupling constants between the EM and weak interactions as follows: $e = g_W sin\theta_W = g' cos\theta_W = g_Z sin\theta_W cos\theta_W$.

However, these fields are defined massless. The Higgs mechanism is the responsible of introducing these mass terms while keeping the EW local gauge invariance.

2.3 Triple Gauge Boson Processes

The SM lagrangian includes gauge boson self-interacting terms and, within the EW sector, triple and quartic gauge couplings (TGCs and QGCs) involving three and four EW gauge bosons respectively. Among these couplings, one of the possibilities is the quartic gauge coupling of the $W\gamma\gamma$ process, depicted in Figure 15 (a), in contrast to the indirect gauge boson interaction in (b). Precision measurements of $W\gamma\gamma$ and other triboson processes allow to look for contributions from physics BSM in the form of anomalous couplings, which so far have not been observed.

Effective Field Theory

A way of studying these couplings and look for potential anomalies is by doing an EFT interpretation. The basis of EFT is its model-independence and the assumption that high-energy physics that are not currently observable by experiments can be approximated to the low-energy regime [21].

Process	$\sqrt{s}$ / TeV	$\int \mathcal{L}dt$ / fb^{-1}	σ / fb	Status
$\gamma\gamma\gamma$ [22]	8	20.2	72.6 ± 6.5 (stat.) ± 9.2 (syst.)	Observed $> 5\sigma$
$WW\gamma$ [23]	8	20.2	1.5 ± 0.9 (stat.) ± 0.5 (syst.)	Evidence 1.4σ
$Z\gamma\gamma$ [24]	13	139	2.45 ± 0.20 (stat.) ± 0.22 (syst.)	Observed $> 5\sigma$
$W\gamma\gamma$ [2]	13	140	$12.2^{+2.1}_{-2.0}$ (stat. and syst.)	Observed 5.6σ
$WZ\gamma$ [25]	13	140	2.01 ± 0.30 (stat.) ± 0.16 (syst.)	Observed 6.3σ
WWW [26]	13	139	820 ± 100 (stat.) ± 80 (syst.)	Observed 8.0σ
WWZ [27]	13	79.8	550 ± 140 (stat.) $\pm\, ^{+150}_{-130}$ (syst.)	Evidence 3.2σ

Table 1: Summary of the measurements of triple gauge boson processes by ATLAS.

Mathematically, it adds certain operators to the SM lagrangian that can be constrained with high-energy precision measurements. These operators are related to the couplings of triple and quartic gauge interactions and thus, could reveal anomalies in these couplings. These EFT interpretations have been ongoing for several analysis by the experiments at the LHC.

Status on Triple Gauge Boson Analyses

When considering a particular process, the *cross section* σ reflects how likely it is to take place. Several SM production cross section measurements have been performed by the ATLAS experiment (see Section 3). In particular, processes involving three gauge bosons are in the lower spectrum of the cross section values with respect to the inelastic cross-section of the initial pp collision.

For the $W\gamma\gamma$ process, the best signal-to-background ratio is obtained by considering the leptonic decay of the W boson, studied in this thesis. This has been recently observed with a significance of 5.6σ by ATLAS [2]. Previously, only evidences of this process were published by both ATLAS and CMS in the LHC [28, 29, 30]. A summary of the current status of this and other triboson processes is shown in Table 1.

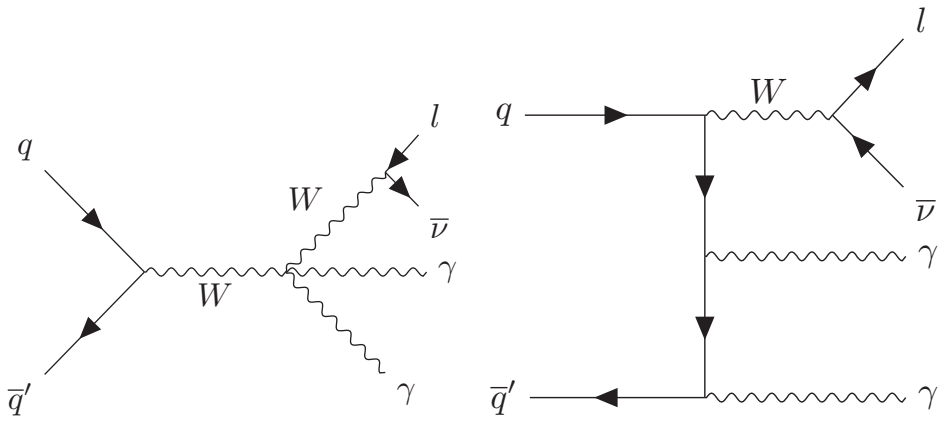

Figure 1: Feynman diagrams for the $W\gamma\gamma$ production at leading order (LO), with the W boson decaying leptonically. In (a) the case of two initial state radiated photons is shown, while in (b) the quartic gauge coupling is depicted.

3 The ATLAS Experiment at the LHC

The Large Hadron Collider (LHC) [31] is currently the world's largest and most powerful particle accelerator. It consists of a 27 km circumference ring [32], located underground at the European Organization for Nuclear Research (CERN) at the border between Switzerland and France. Two high-energetic particle beams are accelerated before being injected into the ring and further accelerated before they collide in particular interaction points. At these interaction points four main experiments are located: ATLAS, CMS, LHCb and ALICE.

In this section, a general overview of the LHC is presented, followed by a more detailed description of the ATLAS detector and its subsystems, since the analysis of this thesis is based on that experiment.

3.1 The Large Hadron Collider

The LHC is designed to collide beams of protons or heavy ions, the former being the relevant collisions studied in this thesis. From the four experiments, ATLAS (A Toroidal LHC Apparatus) and CMS (Compact Muon Solenoid) are general purpose detectors and are built for precision measurements of the Standard Model, including the discovery of the Higgs boson in 2012, and searches for physics beyond the SM. Regarding the remaining two, the LHCb (LHC-beauty) focuses on b quark measurements in order to understand the difference between matter and antimatter, while ALICE (A Large Ion Collider Experiment) is dedicated to heavy-ion physics and the study of the quark-gluon plasma formation at extreme energy densities.

Before the proton-proton collisions in the main acceleration ring, the protons are accelerated through a chain of pre-accelerators until they reach energies of 450 GeV. At this point they are injected into the LHC where they are further accelerated to 6.5 TeV [33]. These beams of protons come in bunches that contain more than 10^{11} protons and they travel in opposite directions along the tunnel until they collide. With a bunch injected every 25 ns, the collisions take place with a frequency of 40 MHz.

The LHC was initially designed to deliver a maximum centre-of-mass energy of $\sqrt{s} = 14$ TeV. Up to now, there have been three data-taking periods at the LHC with increasing centre-of-mass energies. The first one delivered pp collisions at centre-of-mass energies of 7 TeV (Run 1, 2010-2012), the second one energies of 13 TeV (Run 2, 2015-2018) and the third one 13.6 TeV (Run 3, 2022-2025). All data analysed in this thesis corresponds to the Run 3 period.

Besides the centre-of-mass energy, another essential property that describes a particle collider is the luminosity. The instantaneous luminosity $\mathcal{L}$ is a measure of the amount of interactions taking place. In the case of the LHC, the expression of the instantaneous luminosity is the following:

$$\mathcal{L} = \frac{n_b N_1 N_2 f_{rev}}{A} \tag{5}$$

i.e. it is proportional to the number of particles in each bunch, N_1 and N_2 and the

number of bunches n_b, the revolution frequency f_{rev}, and inversely proportional to the beam cross-section, A. This means that in order to achieve a higher instantaneous luminosity, more particles have to be added to the beam or the beam has to be focused more tightly.

When a particular period of data-taking is considered, the integrated luminosity is then used: $L_{int} = \int \mathcal{L} dt$. It is a measurement of the size of the collected dataset. Taking into account a particular process, the number of events is given by $N = \sigma L_{int}$, where σ is the cross section of the process. For Run 2 a total $L_{int} = 140$ fb^{-1} was available, while by the time this thesis was written, Run 3 had delivered $L_{int} = 59$ fb^{-1}, corresponding to the first two years out of the three. However, by the end of Run 3, the luminosity, as well as the centre of mass energy $\sqrt{s}$, will have increased with respect to Run 2.

With increasing luminosity, different pp collisions can overlap within a bunch crossing, since pairs of protons can collide simultaneously. This phenomenon is known as *pile-up*, and it is particular challenging at particle reconstruction. For Run 2, the average number of simultaneous interactions per bunch crossing $\langle \mu \rangle$ was 33.7, while for Run 3 it increased, never exceeding 60.

With the future Run 4, the LHC will enter the new High Luminosity (HL-LHC) era, for which the integrated luminosity will be 10 times higher than the initial design value. With this in sight, the experiments have to be upgraded progressively. Alternating the data-taking periods, the experiments in the LHC go through long shutdown periods where major upgrades are introduced. As explained in the following section, the ATLAS detector introduced some upgrades during its second maintenance period, known as Long Shutdown 2 (LS2), which lasted from 2018 to 2021 and where the detector is gradually preparing for the luminosity increase.

3.2 The ATLAS Experiment

The ATLAS experiment is a collection of sub-detectors with an onion-shape structure situated in a cavern at 100 m below ground. It has a cylindrical shape with a length of 46 m and diameter of 25 m, with an overall weight of approximately 7000 t. The full system is shown in Figure 2.

The different subsystems surround the beam pipe concentrically and thus it consists of a forward-backward symmetric detector with respect to the interaction point. The innermost part is the inner detector, followed by the electromagnetic and hadronic calorimeters and all of it is surrounded by the muon spectrometer. Moreover, several magnets are placed at different locations inside the detector. The magnet configuration consists of a superconducting solenoid magnet that wraps the inner detector, and three superconducting toroids (the barrel and the two end-caps) that surround the calorimeters.

Due to the particular placement of the subdetectors within the ATLAS experiment, a special coordinate system is defined in order to describe the particles of interest. The z-axis points along the beam pipe, the x-axis to the centre (the origin of the nominal collision point) and y-axis in the upward direction. The x and y axes define

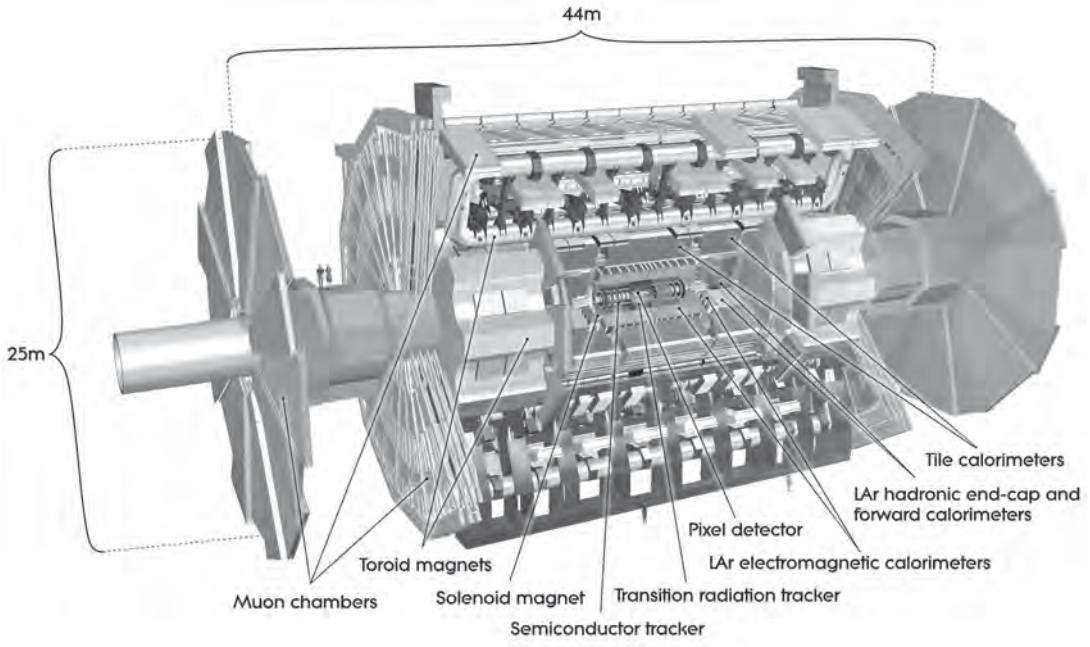

Figure 2: Layout of the sub-detectors in the ATLAS experiment. Image taken from [34].

the transverse plane, the three of them being perpendicular between each other. The two main spatial coordinates are the azimuthal angle ϕ around the beam pipe and the pseudorapidity η. The latter is defined in terms of the polar angle θ as

$$\eta = -\ln\left(\tan\frac{\theta}{2}\right). \tag{6}$$

It covers a range from $\eta = 0$, which corresponds to a particle travelling at $\theta = \pi/2$, i.e. orthogonal to the beam pipe, to $\eta = \pm\infty$, in the case of a particle flying with its momentum aligned to the beam direction[5]. The transverse momentum p_T is a commonly used quantity that measures the momentum of a particle in the transverse plane and it is highly convenient since the overall transverse energy is conserved in the detector. For this reason, the three main quantities that define a particle within the detector are p_T, η and ϕ.

Regarding the specific role that each sub-system of the detector plays in the particle detection, a brief description will be given, starting with the innermost component towards the outermost. First of all, the inner detector is dedicated to momentum, charge and vertex measurements. It is immersed in a 2 T field and covers a range up to $|\eta| < 2.5$. The ID is further divided into three components, from which the Pixel Detector (PD) is the one closest to the interaction vertex. It is followed by the Semiconductor Tracker (SCT) and the Transition Radiation Tracker (TRT). The PD has the highest spatial resolution, which allows vertex reconstruction, while the SCT has a better momentum resolution due to the fact that it has more layers and thus

[5]ATLAS instrumentation reaches up to $|\eta| = 4.9$

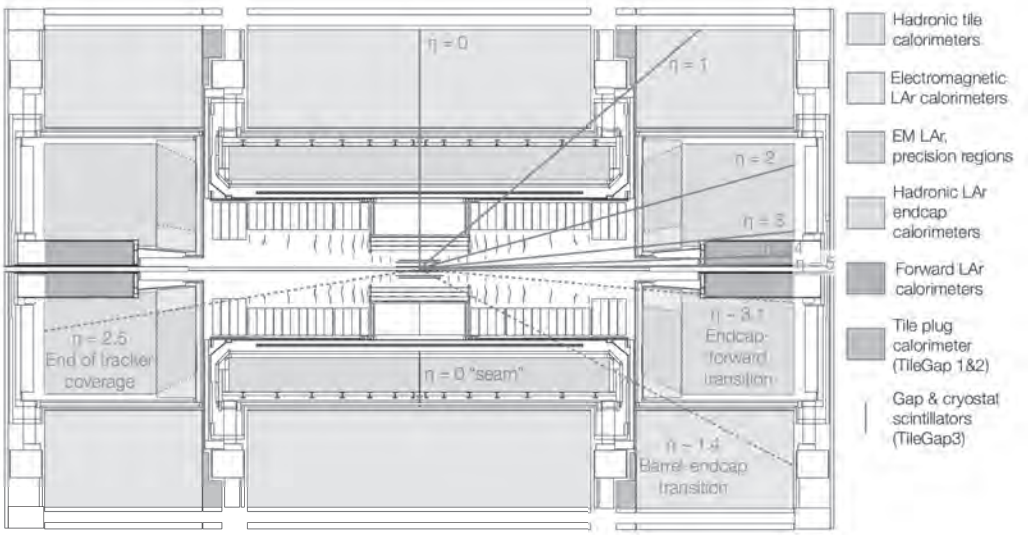

Figure 3: Layout of ATLAS calorimeters with the η values. Image taken from [35].

more space points used for track fitting. Both of them are divided in different layers that fall in the barrel region as well as the end-cap region. The TRT provides an initial particle identification relying on the characteristics of the transition radiation emitted and measured within this subdetector.

In the next layer of the ATLAS detector there is the Electromagnetic Calorimeter. As its name suggest, it is dedicated to contain photons, electrons and positrons that therefore would not continue to further layers of the detector. The next one, the Hadronic Calorimeter, follows the same principle but regarding hadrons. Both of them are sampling calorimeters, with high resolution on energy and position measurements, and are composed of alternating layers of absorber and active media. Liquid argon, LAr, is used as active medium in the EM Calorimeter and the end-caps, while in the Hadronic Calorimeter scintillating tiles are used. The goal is to induce electromagnetic or hadronic cascades in the absorbers and subsequently record the energy deposits in the active media through ionisation or scintillation.

In Figure 3, the η coverage of the ATLAS Calorimeters is depicted. In the case of the Electromagnetic Calorimeters, two regions in η are covered: up to $|\eta| < 1.475$ in the barrel, divided into three layers with different η and ϕ granularity, and between $1.375 < |\eta| < 3.2$ in the end-caps. Most of the energy is deposited in the second layer of the EM Barrel Calorimeter. On the other hand, the Hadronic Calorimeter covers $\eta < 1.7$ with the Tile Calorimeter, while the other part in the end-cap region covers the range $1.5 < \eta < 3.2$. At the end of the calorimeter system, the Forward Calorimeter is placed, covering $3.1 < \eta < 4.9$ in the end-cap region. This coverage in η has an impact particle identification and transition regions are typically excluded in offline analysis due to inefficiencies in the reconstruction.

The outermost part of the ATLAS detector is the Muon Spectrometer (MS). This is due to the fact that muons are usually minimum ionizing particles and thus leave

low energy depositions in the calorimeters. The system consists of three layers in the range of $|\eta| < 2.7$ and they are alternated with three large superconducting toroid magnets. The bending effect of the muons is measured by the different subdetectors within the MS, being particularly precise in η measurements. It is also divided in barrel ($|\eta| < 1.05$) and endcap ($1.05 < |\eta| < 2.7$) regions. In the barrel region a good muon vertex identification is archieved and the muon trigger receives information from it, as well as from the endcap region up to $|\eta| = 2.4$.

Trigger and Data Acquisition (TDAQ) System

At the LHC, the proton bunches collide with a frequency of 40 MHz with multiple *pp* collisions taking place simultaneously, previously introduced as pile-up. The information given from a particular bunch-crossing interaction is called *event*, and it is the most basic level in the physics analysis. The data have an average size of 1.6 MB per event and aiming to store all of this information would imply a waste of resources and would technically not be possible, since not everything is of interest for the physics analysis and it would translate in storing 60 GB/s. For this purpose, the ATLAS detector has a trigger system that decides which events to save.

The ATLAS trigger system is divided into two levels. The first one, the Level-1 (L1) trigger, is a hardware-based system that reduces the rate from 40 MHz to 100 kHz. The second level is the software-based High-level trigger (HLT) and reduces the rate further to 1 kHz. The L1 trigger uses the information of the energy deposited in the calorimeters and in the muon chambers. A first selection of candidates is performed by the L1 Calorimeter Trigger (L1Calo), where candidates of photons, electrons, taus and jets must pass certain energy thresholds and/or isolation requirements. In parallel, the L1 Muon trigger (L1Muon) selects the muon candidates with conditions on the transverse momentum of tracks of the candidates. The next step is the combination of the information received by L1 Calo and L1 Muon by the Level-1 Topological Trigger (L1 Topo). As its name suggests, topological relations are determined at this level, e.g. the angular distance between the objects, using the kinematic information from objects reconstructed in the previous steps. All of this information is then forwarded into the Central Trigger Processor, where the trigger decision takes place.

In the second level of the ATLAS trigger, the HLT receives the events accepted by the L1 trigger and the full detector information is used in order to perform a particle reconstruction in two steps. In addition, there are two possibilities for the particle reconstruction, it either takes place in certain $\eta - \phi$ regions, called *Regions of Interest* (ROIs), or in the whole calorimeter using the missing transverse energy out of momentum conservation laws. In the two steps of the HLT particle reconstruction a fast event rejection takes place first, followed by an offline-like (physics analysis) particle reconstruction.

The latency of the HLT is higher than the one of the L1 trigger, the former being of the order of seconds and the latter of the order of micro seconds. Finally, the Data Acquisition (DAQ) System transfers data from the particular subdetector electronics which is stored permanently in the Tier-0 data centre, from where it is later processed

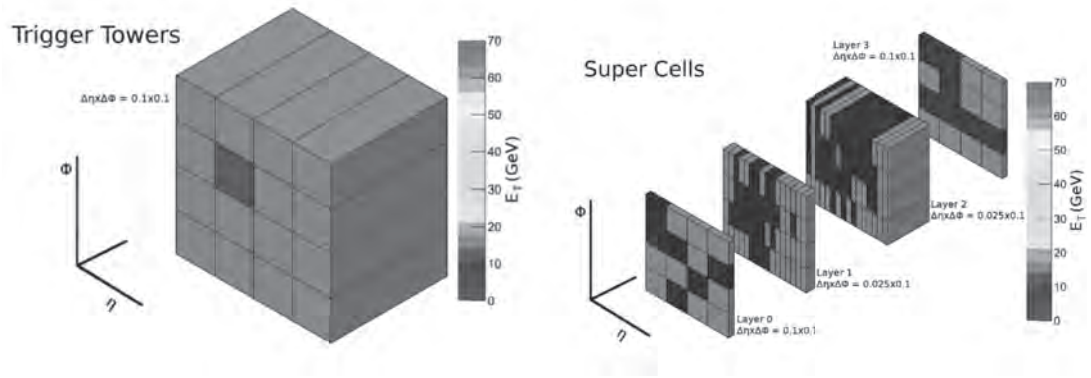

Figure 4: Signatures of an electron with an energy of 70 GeV in both Legacy Trigger Towers (left) and Phase I SuperCells (right) [36].

into different data formats used for offline analysis.

Level-1 Trigger and Run 3 Upgrades

With the increase of centre of mass energy and luminosity in the ongoing Run 3 of the LHC, more *pp* collisions and subsequently more pile-up is expected. In this new environment, an upgrade of the previous L1 trigger system - the Legacy system - was needed in order to minimise the rate of events being recorded, while maintaining high and unbiased efficiency for the interesting processes. These upgrades, referred to as Phase-I Upgrade, were introduced during the Long Shutdown 2 (2019-2022), before the Run 3 of the LHC started.

In the Legacy system, the energy deposited longitudinally in the cells of the calorimeter were summed in *Trigger Towers* covering an area of $\Delta\eta$x$\Delta\phi$ = 0.1x0.1. In the Phase-I system, each trigger tower contains now 10 *SuperCells*, which sum up four or eight calorimeter cells. An additional splitting on the longitudinal axis is done, having a total of four layers with varying granularity in η, where the middle two layers cover an area of $\Delta\eta$x$\Delta\phi$ = 0.025x0.1 [36]. In Figure 4, the differences between the Legacy trigger towers and the Phase I Super Cells are depicted.

A major upgrade at this step of the trigger system is the digitisation of the input of the L1 Calo system. For Legacy, the L1 Calo system was receiving the information from the trigger towers analogically. Now, in the Phase I system, this input is digitised by new LAr Trigger Digitiser Boards (LTDB) before being fed to L1 Calo. However, an analogue conversion is also performed by the Trigger Builder Board (TBB) in order to maintain the Legacy system working in parallel [37] and the Tile Calorimeter is still sending analogue trigger tower signals. These and the following upgrades are depicted in Figure 5.

In the Legacy system, the trigger tower data was first digitised and the energy was reconstructed in the *Pre-Processor Module* (PPM), before being sent to the Cluster processor (CP) and the Jet Energy Processor (JEP) systems for a first object recosntruction algorithms. In the Phase-I system, once the Super Cell transverse energy

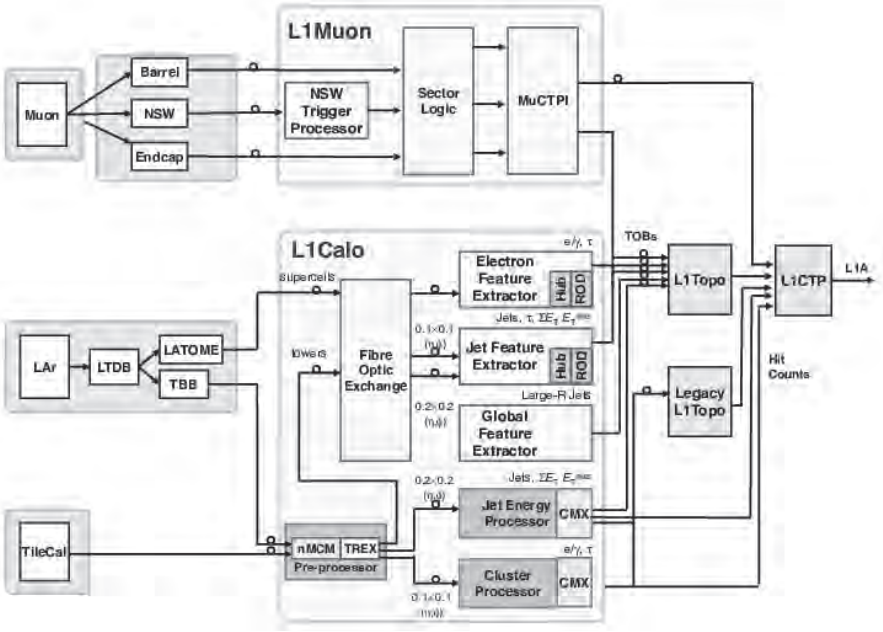

Figure 5: Schematic overview of the upgraded trigger system. The Legacy system components are shown in green, while the Phase-I added components are shown in yellow. Image taken from [38].

is obtained and digitised, it is transmitted to the L1Calo feature extractors (FEXs): the electromagnetic (eFEX), jet (jFEX) and global (gFEX) feature extractors. The most relevant processor for this analysis is the eFEX and it is dedicated to reconstruct electromagnetic objects and hadronically decaying tau-leptons. The identification of these objects is done by the use of shower-shape variables that define three threshold parameters for the EM triggers: *loose*, *medium* and *tight*. More details on these triggers are given in Section 6.1.

The information of the Tile Calorimeter is now also distributed by the Tile Rear EXtension (TREX) modules and then sent to both the Legacy L1 Calo Processors and the new Phase-I FEXs. In parallel, the L1 Muon system was also upgraded with the introduction of the new small wheels (NSWs) in the innermost MS station, along with the upgrade of the MUCTPI.

High-Level Trigger reconstruction and Physics Triggers

If an event is accepted by the L1 Trigger, the information where the candidates were identified, either in the full detector volume or in restricted ROIs, is sent to the HLT Trigger [39]. In contrast the hardware-based L1 Trigger, the HLT is software-based and it uses the same framework as in offline reconstruction (see Section 4.3).

In the very first steps, the HLT Trigger performs track reconstruction by requesting the information from the inner detector within the ROIs. First, a fast-track fit is done, followed by a precision-track fit that refits it by making use of offline track reconstruction

algorithms. More details on the track reconstruction can be found in [40].

In parallel, the HLT calorimeter (HLTCalo) software reconstructs energy clusters for the candidates and also shower-shape variables that are helpful in particle identification. This is done by the topological clustering algorithm [41]. More details on particle reconstruction are given in Section 4.1.

Several sets of requirements define the physics triggers that give a first hint of which particles are participating in the event. Each combination of conditions is included in *trigger chains* (see Section 6.1), which can refer to one or multiple objects within an event, and the whole set of triggers defines the *trigger menu*.

The upgrade on the trigger system from Legacy to Phase-I not only implied changes in some of the pre-established trigger conditions, but also in the naming conventions of the trigger chains. Both the Legacy and Phase I systems still coexisted during the early Run 3. During the first year of the Run 3 (2022), the Legacy system was still enabled, while the Phase-I system was switched on at the end of the year. Therefore, a comparison of the trigger performance for both systems used in this analysis is performed for the first two years of Run 3 (see Section 6).

4 Particle Reconstruction and Monte Carlo Simulations

The basis of the identification of particles produced in *pp* collisions is the understanding of their interaction with the different subsystems of the detector. Leaving the neutrinos aside, particles leave signatures in the form of energy deposits. This traces are then used by several dedicated algorithms to reconstruct tracks and calorimeter clusters, which are the basic characterisation of the particles. This association is then combined with extra topological requirements that enhance the reconstruction, such as isolation conditions and background rejection. This happens both at trigger level by the HLT trigger, referred as *online* reconstruction, and at analysis level, called *offline* reconstruction, the latter being more exhaustive.

Another important part of particle reconstruction is the comparison of real recorded data with simulations. It is essential to understand how processes that are theoretically predicted can be actually measured, in order to compare them to the expectations and improve the predictions. In the following section a summarised description of the relevant particle reconstruction algorithms in the ATLAS detector is given, along with a brief introduction of Monte Carlo (MC) Simulations. Lastly, the framework and data formats used in the ATLAS experiment are introduced.

4.1 Particle Reconstruction Algorithms

The very first steps of particle identification from the detector information are the reconstruction of interaction vertices and tracks, in the case of charged particles, as well as the reconstruction of energy deposits in the calorimeter cells. Regarding vertices, two types are distinguished: the primary vertex, where a particular *pp* collision lead to the production of the particles of interest, and secondary vertices, which are less-energetic decay products or pile-up processes.

Electron and Photon reconstruction

The reconstruction of electrons and photons is done by the same algorithm based on following the EM showers in which they are both involved. In the case of the electrons, since they are charged, track reconstruction is possible. On the other hand, photons do not produce any tracks, but since they can potentially convert into electron-positron pairs and subsequently these emit bremstrahlung, this radiation can be used for the reconstruction.

The first step in electron and photon reconstruction is the track and cluster association, which is done by a set of different algorithms. A *4-2-0 clustering algorithm* [42] follows the development of the EM showers by selecting *topological clusters* or simply *topo-clusters*, which are clusters of energy deposits of topologically close-by EM calorimeter cells. They are chosen when the energy deposit $E_{\text{cell}}^{\text{EM}}$ exceeds certain noise threshold $\sigma_{\text{noise}}^{\text{EM}}$ [41]:

$$\chi^{\mathrm{EM}}_{\mathrm{cell}} = \frac{E^{\mathrm{EM}}_{\mathrm{cell}}}{\sigma^{\mathrm{EM}}_{\mathrm{noise,\ cell}}} > S \tag{7}$$

where S is the seeding parameter. The cluster seed has to exceed $\chi^{\mathrm{EM}}_{\mathrm{cell}} \geq 4$. This condition extends to neighbouring cells successively, turning into seeding cells if they exceed $\chi^{\mathrm{EM}}_{\mathrm{cell}} \geq 2$. Once this condition is not fulfilled anymore, the surrounding cells are added, with $\chi^{\mathrm{EM}}_{\mathrm{cell}} \geq 0$.

In the case of the electrons, since they are charged particles it is required to have a match of a tracks with the topo-cluster. The next step is forming *superclusters* out of single or several track-matched topo-clusters, which is done in a dynamic way and varies in size in order to account for different shower developments. At this step, initial position corrections and energy calibrations are applied to the superclusters, and a final matching of tracks and superclusters is performed [43].

In parallel, photons are also reconstructed from topo-clusters, but since they do not leave any tracks in the inner detector, their conversion into electron-positron pairs is exploited. Once a topo-cluster is selected, these conversion vertices are reconstructed and matched. After this, the superclusters are formed in the same way as the electrons and the conversion vertices are matched the photon superclusters.

After the electron and photon supercluster reconstruction, ambiguities between them are resolved by the algorithm. Depending on the track-to-supercluster fit, the result of the algorithm can be electron-only, photon-only or ambiguous. This information is used afterwards in the offline reconstruction, where again certain calibrations are needed.

Both tracks and EM topo-clusters are reconstructed for $|\eta| < 2.47$. Most of the energy deposited is located in the second layer of the EM calorimeter with no significant leakage into the hadronic calorimeter. In order to improve the selection, several quality criteria are used. These are referred to as *identification* (ID) criteria and rely on a likelihood discriminant built from quantities measured in the inner detector, the calorimeter and both combined. Different identification working points (ID WPs) are defined based on the quality of the inner detector tracks, shower development in lateral and longitudinal directions and cluster-track position association. Similarly, different ID WPs are defined for the photons, but in this case the definitions rely on rectangular cuts on shower-shape variables.

However, this information is still not enough for a final particle identification. For example, high-energetic jets can produce a signature that mimics photons or electrons, and therefore there can be a mis-identification. These mis-reconstructed particles are commonly known as *fakes*. Additionally, within the context of a process of interest, the desirable particles are the *promptly* produced particles, while other contributions from secondary or overlapping processes, i.e. *non-prompt* contributions, want to be suppressed. A more detailed explanation of these different contributions is given in Section 7.1, in the context of the $W\gamma\gamma$ analysis.

The first step to suppress mis-identified particles is to examine the surroundings of the particle and studying how isolated it is from other objects. This is done by taking into account the tracks of close-by charged particles or energy deposits in the

calorimeters [44]. While prompt electrons and photons are expected to be isolated, non-prompt ones usually have remnants of jets in their surroundings. Two types of isolation can be distinguished:

- Calorimeter isolation, E_T^{coneXX}: Uses the measurement of the energy deposits from the calorimeter clusters. Defining a cone around the barycentre of the particle for a certain radius[6], it sums up the energy of the topo-clusters included within the cone. To the raw calorimeter isolation $E_{T,\,\text{raw}}^{\text{isolXX}}$, the EM particle energy, other objects and pileup objects are subtracted:

$$E_T^{\text{coneXX}} = E_{T,\,\text{raw}}^{\text{isolXX}} - E_{T,\,\text{core}} - E_{T,\,\text{leakage}} - E_{T,\,\text{pileup}} \tag{8}$$

  A visual representation of how these isolation cones look in the η, ϕ plane including different energy clusters is shown in Figure 6 (a).

- Track isolation, p_T^{coneXX}: In this case the transverse momenta tracks within the defined cone around the electron track or the photon cluster are summed, excluding the matched tracks to the electron or converted photon. A simplified depiction of the track isolation cones is shown in Figure 6 (b).

  In the case of electrons, the cone has a variable size to account for the differences depending on how the electron was produced:

$$\Delta R = \min\left(\frac{10}{p_T\,[GeV]},\, \Delta R_{\text{max}}\right), \tag{9}$$

  with ΔR_{max} being the maxium cone size, which is typically 0.2. If the particle decaying into an electron has a high-momentum, other decay products are expected to be close to the electron direction. Therefore, the cone shrinks in the case of a high-momentum electron.

Several working points are defined for these isolation variables, depending on the characteristics of the final states that are examined in the corresponding analysis.

Muon reconstruction

The reconstruction of muons [46] is done by combining the information from the inner detector and the MS. The fit of the hits from the inner detector and the MS tracks is enough in the majority of the reconstructed muons. The remaining ones are formed by tagging ID tracks with muon signatures in the calorimeter or the MS. In this case four tags are distinguished: Segment-tagged (ID and first MS stations), Calo-tagged (ID and calorimeter), Stand-alone (only MS) and Combined (all parts involved). According to the quality level of the track fitting for the different tags and the kinematics (p_T and η cuts), different WPs are defined. For instance, muons produced in hadronic decays

[6]The cone is defined in the η, ϕ plane and its typical values are 0.2 or 0.3. The notation XX refers to $\Delta R = \text{XX}/100$

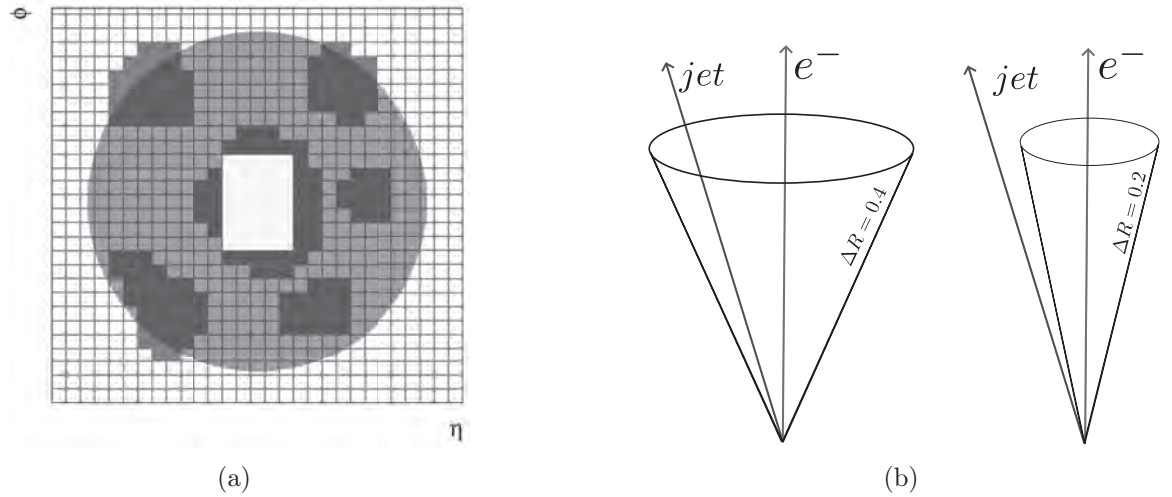

(a) (b)

Figure 6: Representation of the concepts of isolation. In (a) the calorimeter isolation is depicted. The image is taken from [45]. In (b) the track isolation is represented in a simplified way for two different cone sizes. The left electron would not be isolated, while the second one, in a tighter cone, would be isolated.

within the inner detector are expected to have a poor quality combined track fit, while prompt muons, such as the ones produced in W boson decays have a better track fit.

Following the concept of isolation introduced in e/γ reconstruction, it can also be applied for muons. Both calorimeter and track-based isolation WPs are defined. While the calorimeter isolation is analogous to the electron and photon one, the track isolation is similar to the electron case but with a variable cone size defined as follows:

$$\Delta R = \min\left(\frac{10}{p_T\,[GeV]}, 0.3\right), \tag{10}$$

in order to improve the performance in the reconstruction of muons coming from high-p_T particles. In addition, track isolation variables with a fixed cone size are also defined.

However, these two types of isolation definition not only complement each other but also have overlapping effects. For example, the track-based isolation offers a better resolution and lower pileup dependence, while the calorimeter-based isolation includes neutral particles that would be ignored by the track isolation estimation. Still, both measure the contributions of charged particles. Therefore, a new algorithm is used in order to reduce the correlation between the two: the *ParticleFlow* or *pflow*-algorithm [47]. In this algorithm, a new variable is introduced as:

$$E_T^{\text{pflow}} = p_{T,\,\text{charged}}^{\text{track-based}} + 0.4 \cdot E_{T,\,\text{neutral}}^{\text{pflow}}, \tag{11}$$

where $E_{T,\,\text{neutral}}^{\text{pflow}}$ includes the contributions of neutral particle flow objects within $\Delta R = 0.2$ around the muon with a weighting factor of 0.4, which is optimised for the rejection of non-prompt muon contributions [48].

Missing transverse energy reconstruction

Only objects that leave traces and therefore can be reconstructed by the particle algorithms have been discussed so far. However, some SM particles such as neutrinos or even BSM particles like Dark Matter remain undetected, even though they also carry transverse momentum. The only way of measuring this is by making use of momentum conservation laws [49], knowing the fraction of transverse momentum that reconstructed particles have.

In this context, two types of reconstructed objects are differentiated. The *hard* objects are the outputs of the reconstruction algorithms, i.e. candidates to be electrons, photons, muons, jets or hadronically decaying taus. The signals that were not identified by the particle algorithms are encompassed in what is called the *soft* term. Therefore, once the hard objects have been reconstructed and calibrated, the missing transverse energy E_T^{miss} from the hard interaction can be estimated through the x and y components:

$$E_{x(y)}^{miss} = E_{x(y)}^{miss,e} + E_{x(y)}^{miss,\gamma} + E_{x(y)}^{miss,\mu} + E_{x(y)}^{miss,jets} + E_{x(y)}^{miss,\tau} + E_{x(y)}^{miss,soft} \tag{12}$$

This assumes the reconstruction of the hard objects, the tagging of pileup objects, the minimisation of mis-identifications and the application of needed calibrations. The construction of the soft term is then done by the use of remaining information from the calorimeters to the tracker that has not been associated to any hard object. This is particularly challenging, since it does not only rely on all of the detector component measurements, but also in the reconstruction algorithms of the hard objects.

At offline analysis level, the missing transverse energy has to be recomputed after the reconstruction of the relevant objects. This means that the objects used for the E_T^{miss} reconstruction can be chosen depending on the analysis. How this is done at this level is explained in Section 7.2.

4.2 Monte Carlo Simulations

In order to test methods and prospects of data analysis and test detector acceptance and performance, simulations are widely used. For a given process, the cross section is first calculated, followed by the simulation of the interactions of the produced particles and the detector.

The total cross section can be factorised as the product of the partonic subprocess cross section and the parton distribution functions (PDFs) of each of the incoming particles [50]. The partonic cross sections can be evaluated at different orders in perturbation theory, where the leading-order (LO) includes the most simple case and next-to-leading order (NLO) include corrections in QED or QCD, i.e. initial and final state radiated (ISR and FSR) particles from the hard process. Everything starts with the generation of the matrix element, which includes the possible quantum transitions between the initial and the final state.

Event generators [50] make use of Monte Carlo (MC) techniques to numerically evaluate the integrals by sampling random numbers from probability density functions that reflect the interacting dynamics.

In *pp* collisions, the simulation starts with the hard process, i.e. the scattering process of the two incoming partons and their energy transfer. Since multiple partons are colliding simultaneously (pile-up), several hard interactions are taking place. Afterwards, all of these produced particles decay, fragment or hadronise into secondary particles. This is included in the event generation as the *underlying events*. In addition there is upcoming electromagnetic or gluon bremstrahlung from initial or final state partons or leptons. These are encompassed in the so-called *parton showers* and they have a dedicated step in the event generation. However, hadronisation processes cannot be treated within the frame of perturbation theory, but rather by empirical-driven methods. This is the reason why such processes are generally not well modelled by MC simulations.

The MC simulation generates events at particle level, commonly referred to as *truth level*, and their interaction with the ATLAS detector using the `GEANT4` simulation toolkit [51]. This includes the effects of the detector response on the variables measured and it digitises the detector information, making the reconstruction of the particles possible, as described in Section 4.1. Regarding event generators, there are several options that include NLO calculations, among which `SHERPA` [52] and `MadGraph` [53] are the most commonly used. Once the particles have gone through all of the steps of the MC simulation, the event reaches the *reconstruction level* in the same format as real recorded events.

4.3 Framework and Analysis Formats

The ATLAS experiment has the Athena software framework [54] for simulation, reconstruction and analysis. Its framework base architecture GAUDI [55] is shared with the LHCb experiment, but the software is specifically used in ATLAS analyses. The structure of Athena allows to configure tools for the analysis via Job Options in python, while the main body is written in C++.

From the raw data obtained from the data acquisition system, the Analysis Object Data (AOD) is obtained, which is further processed into Derived Analysis Object Data (DAOD). The basic structure are containers. For instance, the `Egamma` container has all of the objects reconstructed with the algorithm dedicated to electrons and photons, which can be further divided into the electron and photon container. In addition to object containers, other types such as the vertex or the event information containers can also be found.

While the AOD contains all of the reconstructed objects, the DAOD might have undergone the following processes [56]:

- Skimming: removal of whole events. E.g. events that do not pass a certain trigger.
- Thinning: removal of whole objects from a container within an event. E.g. objects

that were not well reconstructed.

- Slimming: removal of branches from all objects in a container, applied uniformly for each event. E.g. a particular variable that is not interesting in an analysis.

All of this is exclusively processed with Athena and it is also used for the whole analysis of this thesis.

Among the DAODs, some are dedicated to particular analyses. There are derivations focused on electron and photon (EGAMXX), jet (JETXX), standard model (STDMX) analysis, etc., where all of the previous are generally skimmed by the requirement of certain triggers. This means that an event pre-selection has taken place and the choice of derivation for a particular analysis would take that into account depending on the relevant data. There are over 80 of these derivations and they are extensively used up until now by physics analyses in ATLAS.

However, these derivations overlap in content and thus it does not provide an efficient way of processing the data [57]. With this major motivation, new analysis formats where introduced for Run 3: PHYS and PHYSLITE DAODs [58]. Both consist of unskimmed datasets and therefore contain all of the trigger decision information. Nevertheless, they have been thinned and slimmed from bad-quality reconstructed objects or variables that are not that useful in later stages of the analyses. The migration to these new formats not only implies a reduction in the space being used, but also provides a more straightforward analysis procedure. In the case of PHYSLITE, which is a prototype for Run 4 analyses, it contains already calibrated object containers, while other derivations and PHYS are non-calibrated. This reduces even more the resources needed and harmonises the analyses at the first stages. It is intented to replace the old derivations in the future. So far, only a few recent analyses have used PHYSLITE [59, 60], since it is still in validation stages.

In this particular analysis, older data formats such as EGAM3 and EGAM4 were used in the beginning. However, some relevant Monte Carlo and data samples became available in PHYSLITE format in the course of the thesis and the analysis framework was adapted to the new format accordingly. This entailed not only the change from the previous naming conventions of containers, but also the adaptation of the established software tools needed in the offline analysis. Using the latest format and latest produced samples introduces this additional difficulty. The framework is being constantly updated, having several versions or *releases*, where tool configurations can change. Moreover, the current recommendations on offline analysis from the developers are usually referred to previous releases that have been validated. This means that the Run 3 analyses recommendations are based on previous analyses from Run 2.

5 Data and Monte Carlo Samples

The analysis is performed using data collected in the first two years of the Run 3 data taking period by the ATLAS detector in pp collisions at $\sqrt{s} = 13.6\,\text{TeV}$. The first year of Run 3, 2022, corresponds to an integrated luminosity of $31.4 \pm 0.7\,\text{fb}^{-1}$ [61], where data-quality requirements have been applied. In the second year, 2023, the integrated luminosity was $28\,\text{fb}^{-1}$ [7]. Taking into account both years, the total luminosity was $59\,\text{fb}^{-1}$.

Data Samples

The full year samples studied were the following:

- `data22_13p6TeV.periodAllYear.physics_Main.PhysCont.DAOD_PHYSLITE.grp22_v03_p5858`
- `data23_13p6TeV.periodAllYear.physics_Main.PhysCont.DAOD_PHYSLITE.grp23_v02_p5858`

As mentioned in Section 4.3, these are PHYSLITE datasets which are already calibrated. However, a preselection step is needed in order to reject possible bad quality data. This is called the *Good Runs List* (GRL), which determine the portions of data that are usable after the subdetector and physics data quality groups within ATLAS have verified them. The GRL chosen for this analysis were the ones recommended by the ATLAS Luminosity Working Group [63].

MC Samples

The signal MC samples corresponding to $W\gamma\gamma$ were not available at the beginning of this thesis. Therefore, a production request based on a first local productions of the sample using `MadGraph` was issued. During the central production of the `MadGraph` sample, two different `Sherpa` samples of the same signal process became available. Even though the main sample used in the event estimation is the first Sherpa sample, the three of them were compared as a validation of the samples and the effect of the different framework releases in which they were produced. All of them consist of next-to-leading order (NLO) samples.

The background samples used in the analysis, corresponding to $Z\gamma\gamma$, $Z\gamma$ and $W(\tau\nu)\gamma\gamma$, were produced with `Sherpa`. These and the signal samples, as well as their relevant details are included in Table 2. All generation filter efficiencies and k-factors[8] are 1.0.

[7] This was obtained with the ATLAS Luminosity Calculator [62]. However, an overall uncertainty has not been yet estimated.

[8] The k-factor accounts for the corrections on cross section calculations, typically from leading order (LO) to NLO.

Sample	DSID	Generator	Athena Release	σ / pb	Sum of Weights
	700870	Sherpa 2.2.14	24.0.12	2.112	$1.21{\cdot}10^{12}$
$e\nu\gamma\gamma$	537421	MadGraph 3.5.1	24.0.21	0.198	$9.45{\cdot}10^{4}$
	700870	Sherpa 2.2.14	24.0.21	2.112	$1.93{\cdot}10^{12}$
$\mu\nu\gamma\gamma$	700871	Sherpa 2.2.14	24.0.12	2.112	$1.06{\cdot}10^{12}$
$ee\gamma\gamma$	700873	Sherpa 2.2.14	24.0.12	1.373	$2.95{\cdot}10^{11}$
$\mu\mu\gamma\gamma$	700874	Sherpa 2.2.14	24.0.12	1.370	$4.99{\cdot}10^{11}$
$ee\gamma$	700770	Sherpa 2.2.14	24.0.12	102.59	$5.68{\cdot}10^{13}$
$\mu\mu\gamma$	700771	Sherpa 2.2.14	24.0.12	102.64	$5.70{\cdot}10^{13}$
$\tau\nu\gamma\gamma$	700872	Sherpa 2.2.14	24.0.12	2.114	$9.91{\cdot}10^{11}$

Table 2: List of all MC samples used in this thesis.

In order to compare MC samples with each other and with a specific dataset and obtain sensible event expectation, the following scaling has to be applied in MC to the number of bare events that pass the selection criteria:

$$S = \frac{\sigma(\text{fb}) \cdot L_{int}(\text{fb}^{-1}) \cdot w_i}{\sum_i^N w_i}, \tag{13}$$

where σ is the cross section of the generated sample, L_{int} the integrated luminosity of the portion of data being considered, w_i the event weight within the sample and all of over the sum of weights of the whole sample. The event weights are applied event-by-event in the intermediate steps of the event selection, while the overall scaling is applied at the end.

6 Trigger Performance Studies

Several triggers, alone or combined, can be used as an initial step in an analysis. For example, if the interest is in a final state where leptons are involved, lepton triggers can be required to ensure that these particles are present in the event. Therefore, the performance of these triggers has a major impact in the analysis and has to be taken into account.

Analyses involving multiple bosons generally make use of single or dilepton HLT triggers. In the particular case of the of the $W\gamma\gamma$ process, three-object triggers involving a lepton - electron or muon - and a pair of photons are available since Run 2. Not only do they involve all of the final state particles in this process, but also have lower thresholds, and thus more accessible phase-space, in comparison to the single and dilepton triggers. Additionally, these triggers are unprescaled[9], meaning that all of the events that fulfil the trigger requirements were stored in the data-taking process.

Moreover, as explained in Section 3.2 , the ATLAS L1 Trigger was upgraded in order to account for the increase of luminosity and pile-up in the new data-taking periods. The old Legacy system was still operative in the first year of the Run 3 (2022), while the Phase-I system was switched on from the full second year (2023) onwards. The guaranty that the two systems have compatible performances is needed in order to verify the proper migration to the new trigger system.

In this section, the performance of the three-object triggers, $l\gamma\gamma$, is presented. First of all, the structure of trigger chains is introduced, as well as the specification of the ones used in the analysis. This is followed by the efficiency calculation strategy and the comparison between the results of the two systems for the two leptonic channels. The main goal of these studies is the verification of the compatibility between the two trigger systems in order to ensure their usage in the $W\gamma\gamma$ analysis.

6.1 Trigger Chains

When talking about triggers in this context, it is referred to the trigger strings that contain the trigger requirements. At the HLT level, they are commonly referred as *trigger chains* and they have always attached a *L1 item*, generally at the end of the string, that acts as seed of the HLT trigger.

Level-1 Items

The beginning of the item is always `L1`. Starting with the Legacy system, in the case of electromagnetic triggers, `EM` is added, followed by a number `XX` that states the p_T threshold and by a group of capital letters that stand for different cuts: `V` means that the p_T threshold varies with η in order to account for energy losses; `H` reflects

[9]Some single-object or low threshold triggers are prescaled to a value n. This means that the number of saved events that fired the trigger is reduced by a factor of $1/n$, i.e. that every n^{th} triggered event is taken.

that hadronic core isolation (no leakage into hadronic calorimeters) is applied; and `I` stands for electromagnetic isolation. An example of this would be `L1EM22VHI`. Different parameters are attached to the muon L1 items, denoted by `MU`. The p_T threshold is shown in the same way, as well as the `V`, followed by other three possible capital letters: `F` requires full-station big wheel coincidence in the endcap; `C` requires inner coincidences for encap (additional coincidence than the previous one); and `H`, for events that have satisfied a good magnetic field for the encap. An example would be `L1MU14FCH`. In any case, the p_T threshold shapes the p_T distribution of the object in a way that it peaks at this value. The corresponding efficiency is characterised by the *turn-on* of the curve around this threshold, i.e. the inflexion point from low to high efficiencies, followed by the plateau, generally reached a few GeV higher, where the efficiency is stabilised and reaches the highest value, ideally one.

With the Phase-I upgrade, the naming convention of the L1 items changed. The starting point, after `L1` accounts for the FEX used (introduced in Section 3.2): `e` stands for eFEX, `j` for jFEX and `g` for gFEX. This is followed again by `EM` in the case of electromagnetic triggers and the p_T threshold. The next information accounts for different combinations of shower shape cuts, which can be `L`,`M` or `T`, reflecting the working points loose, medium and tight and that have similar performance than the Legacy variable combinations. An example of a Phase-I item would be `L1eEM26M`. The muon triggers have not changed the name convention significantly. However, new requirements have been added in order to restrict more the regions within the muon stations.

In both cases this can be extended to multiple object triggers. This appends to the initial L1 item a string with a similar structure as the main one, but adding the multiplicity in front of the trigger type. An example is `L1EM22VHI_3EM10VH`, which consists of a three object L1 item, where the three items pass the p_T of 10 GeV and `VH` conditions and, additionally, one of the items passes the higher threshold of 22 GeV and an extra condition `I`. This is similar for Phase-I, following the corresponding notation.

HLT Chains

The previous L1 seeds are appended to the HLT name in order to have the final HLT chain. The HLT part starts with the name `HLT`, followed by the type of object, always in lower case, and the p_T threshold: electron `eXX`, photon `gXX`, muon `muXX`, etc. Then, depending on the object, different identification and isolation working points are attached. These can be compared to offline working points and a harmonisation between offline and online is necessary on order to avoid any bias.. An example from the $W\gamma\gamma$ analysis of an HLT chain would be `HLT_e26_lhtight_ivarloose_L1EM22VHI`, where `lhtight` stands for the ID WP and `ivarloose` for the isolation WP. This is similar for photons and muons, with different WPs definitions.

The multiplicity of the HLT object or the combination of different type objects is also possible. This is reflected by adding the multiplicity number before the object type by attaching the HLT component one after the other. An example would be a three object trigger in the Legacy system: `HLT_e24_lhmedium_g12_loose_g12_loose_02dRAB_02dRAC_02dRBC_L1EM20VH_3EM10VH`, where an electron and two photons define the trigger

Objects	Legacy system	Phase I system
Single e	HLT_e26_lhtight_ivarloose _L1EM22VHI	HLT_e26_lhtight_ivarloose _L1eEM26M
$e\gamma\gamma$	HLT_e24_lhmedium _g12_loose_g12_loose _02dRAB_02dRAC_02dRBC _L1EM20VH_3EM10VH	HLT_e24_lhmedium _g12_loose_g12_loose _02dRAB_02dRAC_02dRBC _L1eEM24L_3eEM12
Single μ	HLT_mu24_ivarmedium _L1MU14FCH	Unchanged
$\mu\gamma\gamma$	HLT_2g10_loose_mu20 _L1MU14FCH	HLT_2g10_loose_L1eEM9_mu20 _L1MU14FCH

Table 3: Trigger chains involved in the efficiency study of the $l\gamma\gamma$ triggers. For the single lepton triggers the unprescaled triggers with the lowest p_T threshold are given. The 3-object triggers are also unprescaled.

chain. Additional topological relations can be added as `02dRAB`, which stands for a distance minimum of 0.2 in the η, ϕ plane between the different combinations of the three objects.

6.2 Trigger Analysis Strategy

The calculation of trigger efficiencies can be done with respect to either reconstructed or truth objects from MC simulations. Typical methods in data are the tag-and-probe or the bootstrap methods [64]. While the first method widely uses a sample of events with a well-know resonance, such as the Z or J/ψ decaying to a pair of charged leptons, the bootstrap method calculates the efficiency with respect to an unbiased or a lower-threshold trigger. The goal is to obtain an unbiased efficiency curve with respect to the kinematic variables, such as the transverse momentum. This is usually done in terms of the lowest-p_T object involved in the process studied.

In the case of the $l\gamma\gamma$, a reference trigger is used. Typically, this trigger should be completely independent to the trigger that is being studied, e.g. a high-p_T jet trigger. However, in this particular case it would heavily reduce the statistics and thus make any sensible turn-on curve not possible. For this reason, the single lepton lowest-p_T triggers were used. This consciously introduces a bias in the efficiency calculation, since the three object trigger includes a single lepton trigger component as well, but with looser requirements. However, these single lepton triggers are studied in depth by the Trigger Performance Groups in the ATLAS Collaboration and present in general a high efficiency [64].

The estimation of the trigger efficiency relative to the single lepton trigger is therefore not necessarily a problem, since the main goal of the analysis is, rather than a full efficiency study of the trigger, the verification of the implementation of the triggers in an analysis and the compatibility between the trigger systems. For this reason, in addition to the trigger efficiency, the trigger *matching* efficiency is also obtained.

Trigger matching verifies whether the selected objects correspond to the combination of particles which actually fired the trigger of interest within the event.

The objects involved in the $l\gamma\gamma$ triggers are the leading and subleading photons and the leading lepton, where leading indicates the highest-p_T objects of that kind. A selection of events which contain these three objects is applied and, at the end, events which have additionally fired the three-object trigger are selected. Since the leading objects are most likely to have fired the trigger, the efficiency is computed with respect to the subleading photon p_T. The efficiency is therefore obtained by dividing the distributions of the subleading photon p_T before and after asking whether the three-object trigger was fired by the event, corresponding to the following expression of the efficiency:

$$\varepsilon_{\text{trigger}} = \frac{N_{\text{fired}}(\text{single } l) \;\&\; l\gamma\gamma \text{ selection} \;\&\; N_{\text{fired}}(l\gamma\gamma)}{N_{\text{fired}}(\text{single } l) \;\&\; l\gamma\gamma \text{ selection}}, \tag{14}$$

i.e. events which fired the $l\gamma\gamma$ triggers, $N_{\text{fired}}(l\gamma\gamma)$, over the events that fired the single lepton trigger, $N_{\text{fired}}(\text{single } l)$, and were subjected to the $l\gamma\gamma$ selection. This efficiency reflects the performance of the $l\gamma\gamma$ triggers.

Additionally, the trigger *matching* efficiency is obtained by making use of the `Trigger Matching Tool` of the Athena framework, which compares the kinematics and topology of offline and online reconstructed objects. The efficiency is then calculated by dividing the p_T distributions of the subleading photons before and after trigger matching, which translates into the following expression:

$$\varepsilon_{\text{matching}} = \frac{N_{\text{fired}}(l\&l\gamma\gamma) \;\&\; l\gamma\gamma \text{ selection} \;\&\; N_{\text{matched}}(l\gamma\gamma)}{N_{\text{fired}}(l\&l\gamma\gamma) \;\&\; l\gamma\gamma \text{ selection}}, \tag{15}$$

i.e. $l\gamma\gamma$ trigger matched events, $N_{\text{matched}}(l\gamma\gamma)$, over all events that fired both the single lepton and $l\gamma\gamma$ triggers and passed the $l\gamma\gamma$ selection. This efficiency therefore reflects how well the trigger identifies the three object combination of a lepton and two photons.

Two separate datasets within Run 3 are used (see Section 5), one corresponding to 2022 data, where the Legacy triggers are tested, and the other one to 2023 data, for Phase-I triggers. The trigger chains used are presented in Table 3, separated in the electron and muon channel and in the two trigger systems. The trigger chains present in each dataset are shown in Figure 7. The same method and event selection, setting the different trigger chain names aside, is applied in both cases.

6.3 Object and Event Selection

First of all, events are required to have fired the lowest-p_T unprescaled single lepton triggers of the corresponding channel. In Figure 8, the transverse momentum distribution of all initial particles after the trigger preselection, photons and electrons for the electron channel and photons and muons for the muon channel are shown. They all reflect the effect of the triggers with the appearance of a peak after the p_T threshold.

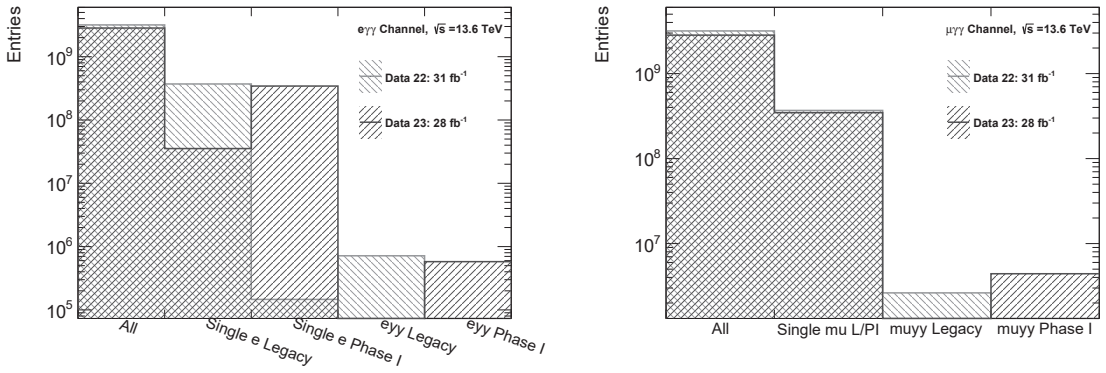

(a) (b)

Figure 7: Relevant trigger chains available in the two datasets used within the Run 3. In (a) the chains involving electrons are shown, while in (b) the muon ones are displayed. In the latter case, the lowest-p_T unprescaled trigger for the Legacy system does not change in the Phase-I system. Both of the diagrams display in the first bin all of the events available, without any trigger pre-selection; the single lepton trigger bins are computed with respect to all of the events; and the three-object trigger bins are counted over the events that fired the single lepton triggers of the corresponding system.

Objects that have a p_T lower than the threshold correspond to secondary objects of the same type which did not necessarily fulfil the trigger conditions. In the case of the photons in the electron channel, in Figure 8 (a), the trigger effect is also present, since this collection of photons might include electrons that were reconstructed as photons. This effect is not present in the muon channel (see Figure 8 (c)).

Since the particle reconstruction algorithms operate in parallel, the possibility of having the same reconstructed object identified as two different particles, e.g. a jet and a photon corresponding to the same detector signals, is quite common. In order to avoid this double counting of objects, an overlap removal is performed on the sets (containers) of reconstructed objects before the individual object selection is applied. This is performed by the `Overlap Removal Tool` of the Athena framework and it compares the particle containers on particle level. A hierarchical removal is done in the following order: electrons sharing an ID track with a muon; photons within $\Delta R < 0.4$ of an electron or a muon; jets within $\Delta R < 0.2$ of an electron; electrons within a $\Delta R < 0.4$ of a jet; jets within a $\Delta R < 0.2$ of a muon; and photons and muons within a $\Delta R < 0.4$ of a jet. Examples of the effects of this overlap removal are shown in the distance plots between pairs of objects in Figure 9.

Several requirements are applied at particle level in order to improve the particle identification. These offline criteria must be harmonised with the trigger conditions in order to not introduce a bias in the efficiency calculation. This is particularly relevant in the case of isolation requirements, where in the latter case the definitions are not fully equivalent.

Photons are required to pass ambiguity requirements, as introduced in Section 4.1,

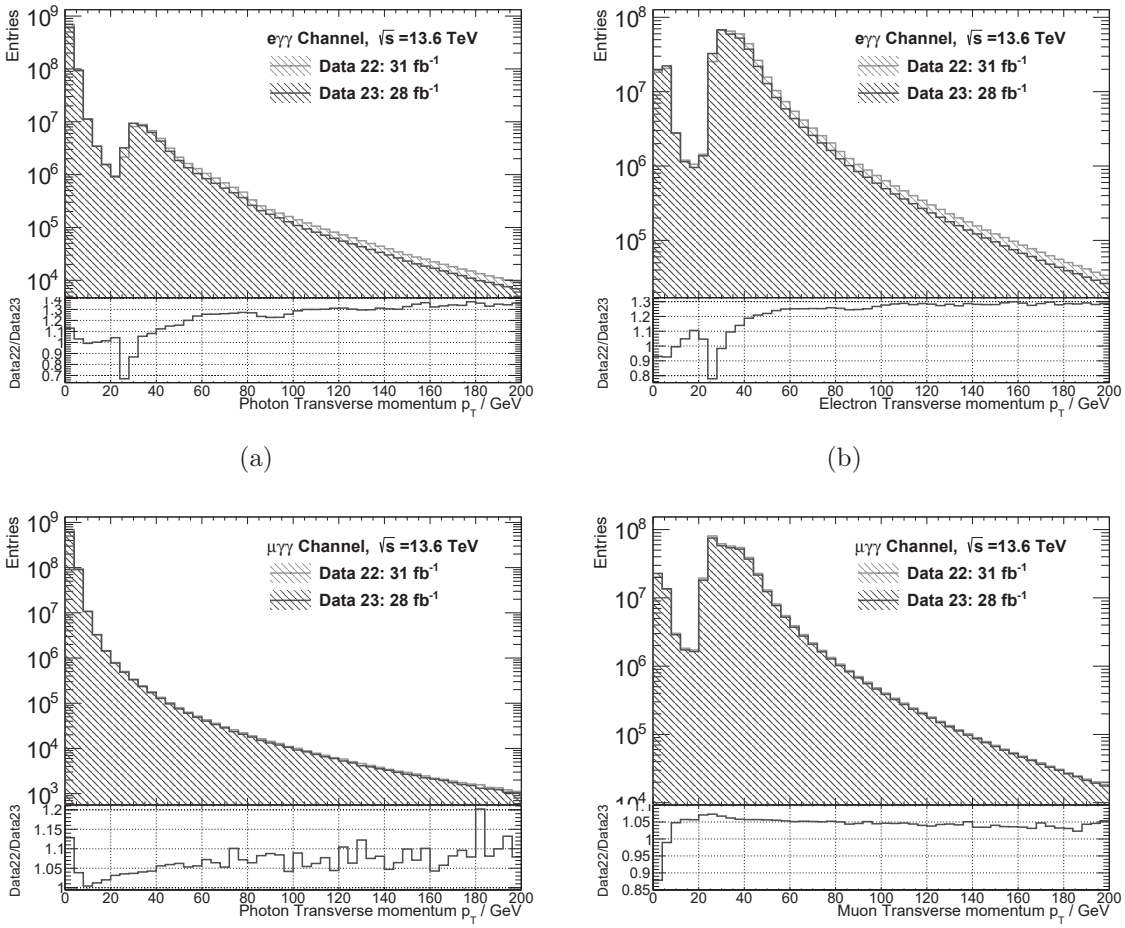

Figure 8: Transverse momentum of the relevant objects after trigger selection and before selection cuts for the two datasets with their respective trigger system. In (a) and (b) the photon and electron distributions for the electron trigger chain is shown; and in (c) and (d) the photon and muon distributions for the muon trigger chain is also shown.

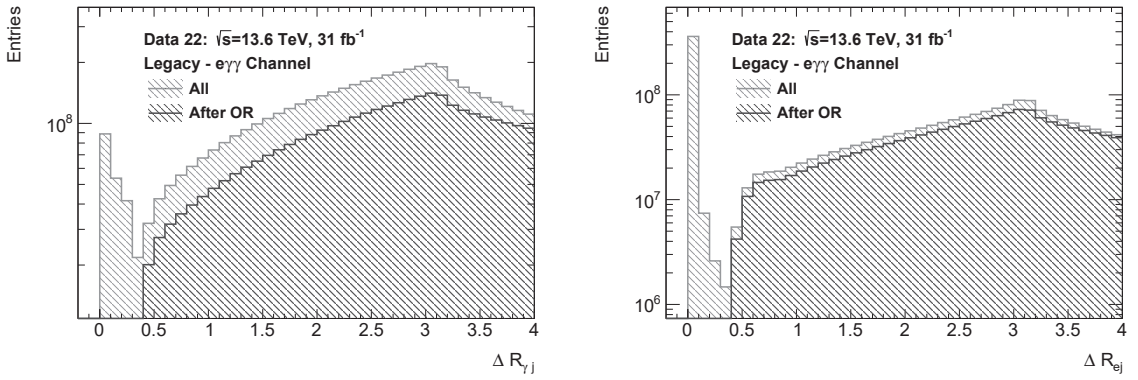

(a) (b)

Figure 9: Distance between objects before and after the effect of the overlap removal (OR), in Data 23 and the electron channel: in (a) photons to jets and in (b) electrons to jets.

and to have a good quality reconstruction of the clusters[10]. Regarding kinematic criteria, they must have a $p_T > 7\,\text{GeV}$ and a $\eta < 2.37$, where the transition region between the EM barrel and endcap regions of the calorimeter, comprising $1.37{<}\eta{<}1.52$, is excluded. The remaining requirements are the identification and isolation WPs. These are set to *tight* identification and to the calorimeter-based tight isolation (*Fixed-Cut Tight Calorimeter Only*[11]) WPs, defined as $E_T^{\text{cone40}} < 0.022\,p_T + 2.45$ [GeV]. Comparing it to the online requirements, the three object trigger component for photons in both electron and muon channel contains the *loose* identification. The choice of tighter identification and isolation requirements responds to the need of reducing the fraction of mis-identified photons. In the case of the p_T, in order to have a complete curve where the turn-on of the trigger and the plateau are well defined, the offline threshold is set to a lower value.

Electrons must satisfy as well ambiguity requirements, since it is part of the e/γ reconstruction algorithm, and a pseudorapidity of $|\eta| < 2.47$, excluding again the transition region $1.37{<}\eta{<}1.52$. They must satisfy that $p_T > 27\,\text{GeV}$[12] and have a loose track-to-vertex association (TTVA), meaning that their track either was used in the primary vertex fit or it fulfils $|\Delta z_0|\,\sin\theta < 3\,\text{mm}$ and $|d_0/\sigma_{d_0}| < 5$. In the first TTVA condition, z_0 is the longitudinal impact parameter, i.e. the distance of closest approach of the track to the primary vertex or beamspot position in the z-axis; as for the second condition, it is a measurement of the track significance based on the transverse impact parameter with respect to the beam line, d_0, and its uncertainty, σ_{d_0}. Additionally, electrons must satisfy the likelihood-based identification working point *lhmedium*, equivalent to the three-object trigger working point, and the *Loose_ VarRad*, which is defined in both calorimeter- and track-based variables as $E_T^{\text{cone20}}/p_T < 0.2$ and $p_T^{\text{varcone30}}/p_T < 0.15$

[10] This information is stored in the derivations as decorations or *flags* on each object.

[11] *FixedCut* stands for rectangular shower-shape cuts.

[12] This choice of the offline p_T threshold potentially removes the effect of the single lepton trigger in the final efficiency curve. This statement is further studied by varying the p_T threshold and comparing the resulting efficiencies.

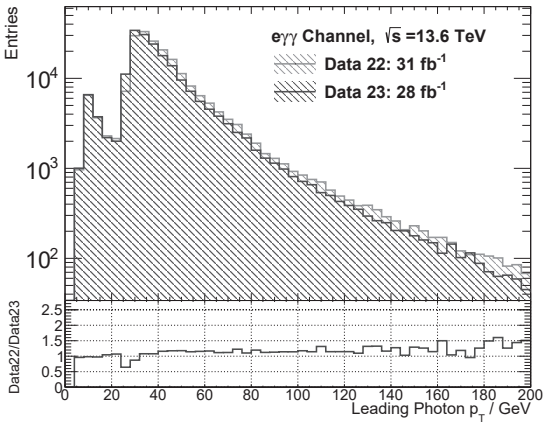

(a)

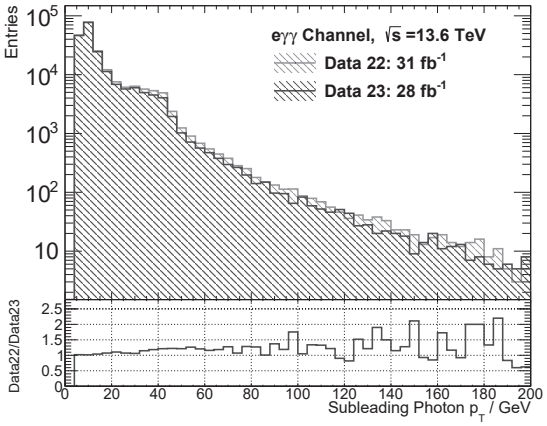

(b)

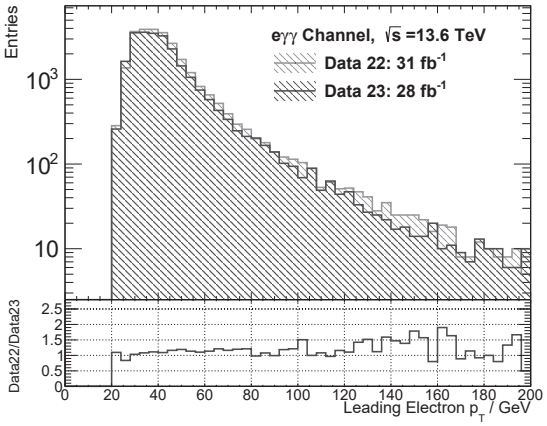

(c)

Figure 10: Transverse momentum distributions of the leading photons (a), subleading photons (b) and leading lepton (c) for the electron channel.

respectively. The isolation working point increases the chances of having a promptly produced electron.

Muons are required to pass good quality reconstruction requirements and the kinematic cuts $|\eta| < 2.4$ and $p_T > 25\,\text{GeV}$. Moreover, they must satisfy the *medium* identification working point and the TTVA requirements of $|z_0 \cdot \sin(\theta)| > 0.5\,\text{mm}$ and $|d_0/\sigma_{d_0}| < 3$. Regarding isolation, the three object trigger muon component does not include any requirement. However, the pflow-based isolation *PflowLoose_VarRad* WP is applied offline in order to restrict them more into prompt muons [13]. The definition of this new concept of isolation was given in Equation 10 and this particular working point fulfils $E_T^{\text{pflow}} < 0.16$.

The distributions of the leading objects are shown in Figure 26 for the electron channel. The leading photon, in Figure 26 (a), still reflects the trigger effect present in the initial distribution. This depicts the fact that the mis-identifications are not completely reduced with identification, isolation or overlap removal criteria. A similar effect is shown in the case of the subleading photon distribution, in Figure 26 (b), where the peak around the trigger threshold is smoother, since it is more likely for a higher-p_T object, i.e. the leading photon, to have fired the trigger. Additionally, the three distributions reflect a good agreement between the two trigger systems and datasets. The muon channel distributions are included in Appendix A.

6.4 Trigger Performance

The overall results of the efficiency of the $l\gamma\gamma$ triggers with respect to the subleading photon p_T are shown in Figure 11. Both Legacy and Phase-I trigger chains are compared for the electron and muon channels. The electron channel trigger efficiency, in Figure 11 (a), shows a good agreement between Legacy and Phase-I systems. Moreover, the values of the efficiency lie above 90% once the plateau of the curve is established. In Figure 11 (b), the results are shown for the muon channel. They show a good agreement between the two trigger systems and an efficiency over 90%.

In order to study the possible effects of the choice of the lowest unprescaled single lepton trigger as reference trigger in the efficiency calculation, the results for different offline p_T cuts on the leading lepton are studied. This is performed for the electron channel for the following p_T values: 20 GeV, a lower p_T than the trigger threshold (26 GeV); 27 GeV, a value slightly above the threshold; and 34 GeV, where a high efficiency of the single electron trigger is expected.

Figure 12 (a) shows the comparison for the Legacy system. The behaviour of the efficiency for the lowest offline electron p_T cut presents differences with respect to the two higher p_T cases. The efficiency shows a tendency downwards for a high subleading photon p_T, which is less prominent with higher electron p_T cuts. However, when comparing the same electron p_T conditions for the Phase-I system, in Figure 12 (b), these differences are not observed. In this case, the three p_T criteria results agree within

[13] *Pflow* working points for muons are recommended in Run 3 analyses by the Isolation Fake Forum. More details on [65].

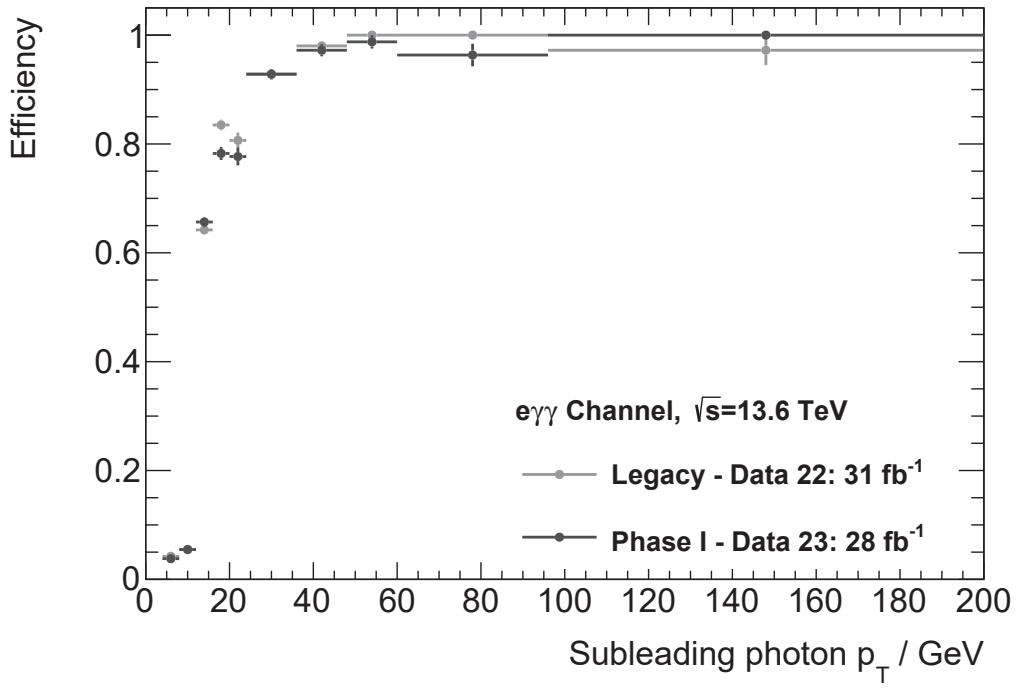

(a)

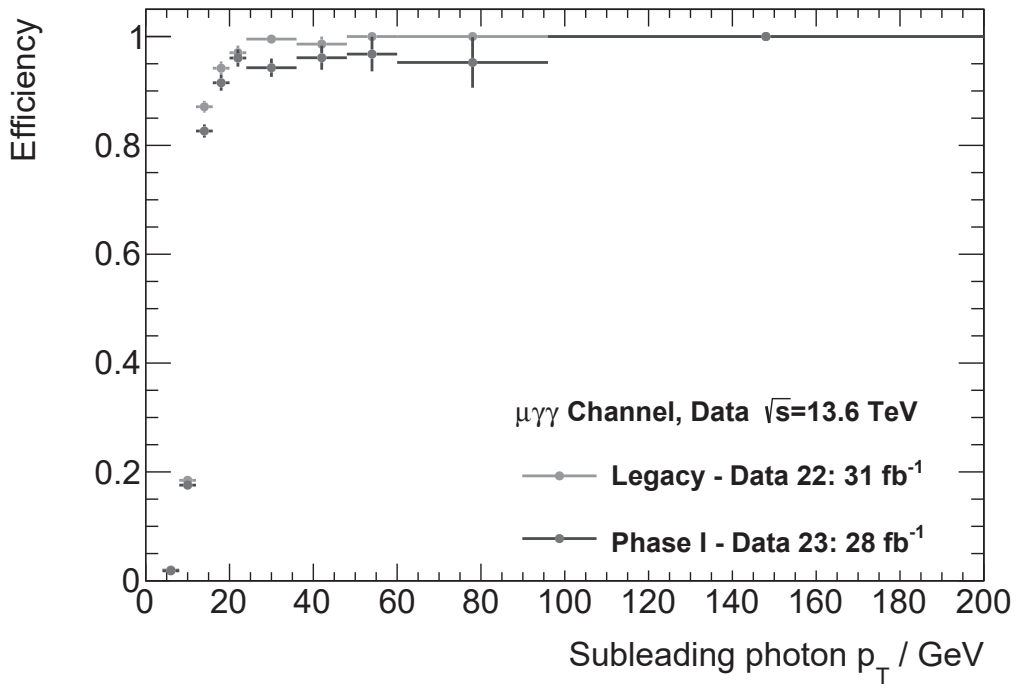

(b)

Figure 11: Results of the trigger efficiencies of the $l\gamma\gamma$ triggers. The results for both the Legacy and Phase-I systems for the $e\gamma\gamma$ trigger chain is shown in (a), while only the Legacy $\mu\gamma\gamma$ trigger results are shown in (b). The error bars represent the statistical uncertainties.

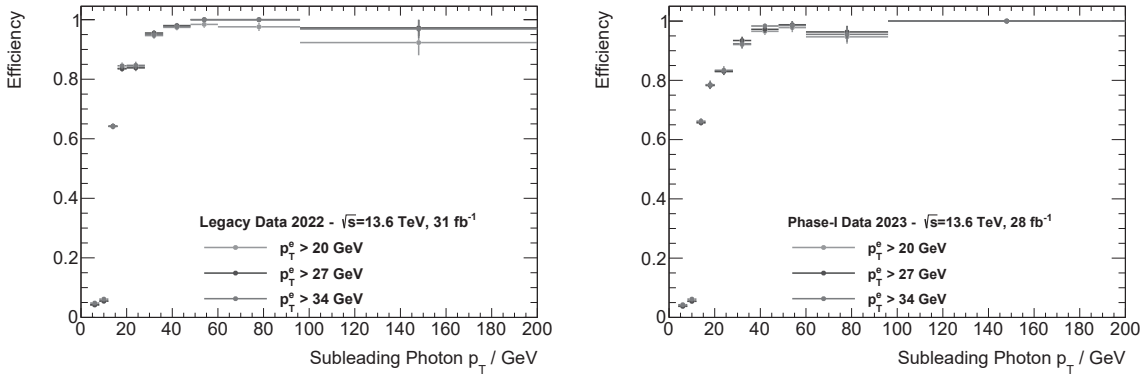

(a) (b)

Figure 12: Results of the trigger efficiencies of the $e\gamma\gamma$ triggers for different offline electron p_T cuts. The comparison for the Legacy system is shown in (a), while the Phase-I system is compared in (b). The error bars represent the statistical uncertainties.

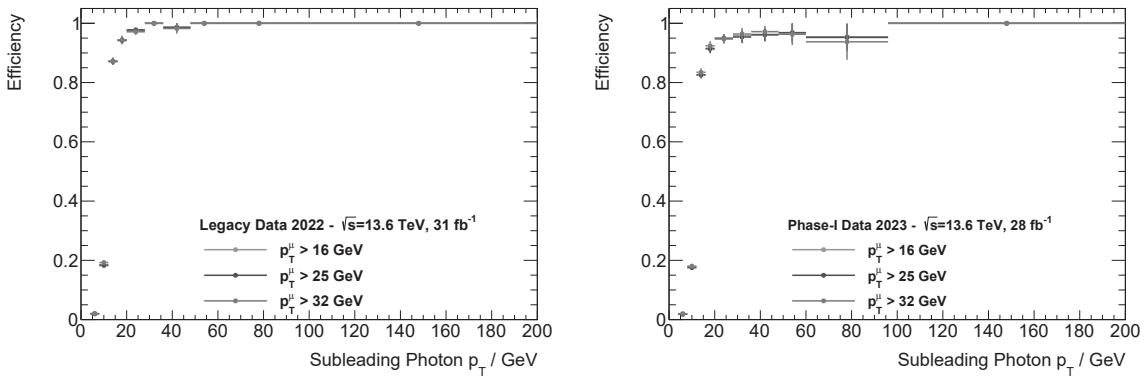

(a) (b)

Figure 13: Results of the trigger efficiencies of the $\mu\gamma\gamma$ triggers for different offline muon p_T cuts. The comparison for the Legacy system is shown in (a), while the Phase-I system is compared in (b). The error bars represent the statistical uncertainties.

the statistical uncertainties. This result justifies the choice of the offline p_T cut on the electron of 27 GeV for further trigger studies, since the efficiency of the three-object trigger is higher in that case and no improvement is shown for higher offline p_T criteria.

An equivalent comparison can be done for the muon channel. In this case, the offline muon p_T values studied were the following: 16 GeV, for a lower p_T than the trigger threshold (24 GeV); 25 GeV, for a value close and above the threshold; and 32 GeV, a value for which a high efficiency of the single muon lepton trigger is expected.

The results for the different offline muon p_T criteria for the Legacy and the Phase-I systems are shown in Figure 13. In the case of the Legacy system, a perfect agreement is shown for the three offline p_T values of the muon, as well as for the Phase-I system, where some differences are found but are in agreement within the statistical uncertainties.

Overall, the results for different offline p_T of the leptons agree with each other. The choice of the single lepton triggers as reference triggers in the efficiency calculation could in principle have an impact when including offline leptons below their threshold. However, the efficiencies are not significantly affected. Further investigation on identification and isolation conditions would be needed in order to discard the impact of the other conditions of the single lepton trigger chain. Additionally, studying the efficiency as a function of the leading lepton would help to quantify the impact of the bias. However, a full study of the performance of the triggers is beyond the scope of this thesis. The high efficiency results and the compatibility between the trigger systems serve as a validation that the usage of these triggers is possible for the search of final states involving two photons and a lepton.

6.5 Trigger Matching Efficiencies

The results of the trigger matching efficiencies for both of the trigger chains are shown in Figure 14. On the first plot, the electron channel trigger chain efficiencies are compared for both the Legacy and Phase-I systems. For these efficiencies, the electron offline p_T cut is set to 27 GeV. A good agreement is shown, with efficiencies over 85% within the statistical uncertainties. On the second plot, the results for the muon channel are shown for the Legacy trigger, where the offline p_T cut of the muon is set to 25 GeV. An efficiency over 80% is shown. In the case of the Phase-I trigger, events had actually fired the trigger, as it can be seen in Figure 7 (b). However, when trying to perform trigger matching with the Phase-I trigger on the three selected objects in this channel, none of the combinations succeeded. It was found out that the `Trigger Matching Tool` was not recognising the muon part of the Phase-I trigger chain and therefore the tool was only requiring two objects (the two photons) to be matched. This problem was reported to the responsible developers of the tool.

These results reflect in the first place that these trigger chains, in the case of the electron channel regardless of the trigger system, have a high efficiency. In spite of the fact that the efficiency is relative to the single lepton trigger efficiencies, which is in any case high, a sensitive test of these triggers is presented, since both the diphoton part and the combination of the three object topology, through ΔR cuts, are studied.

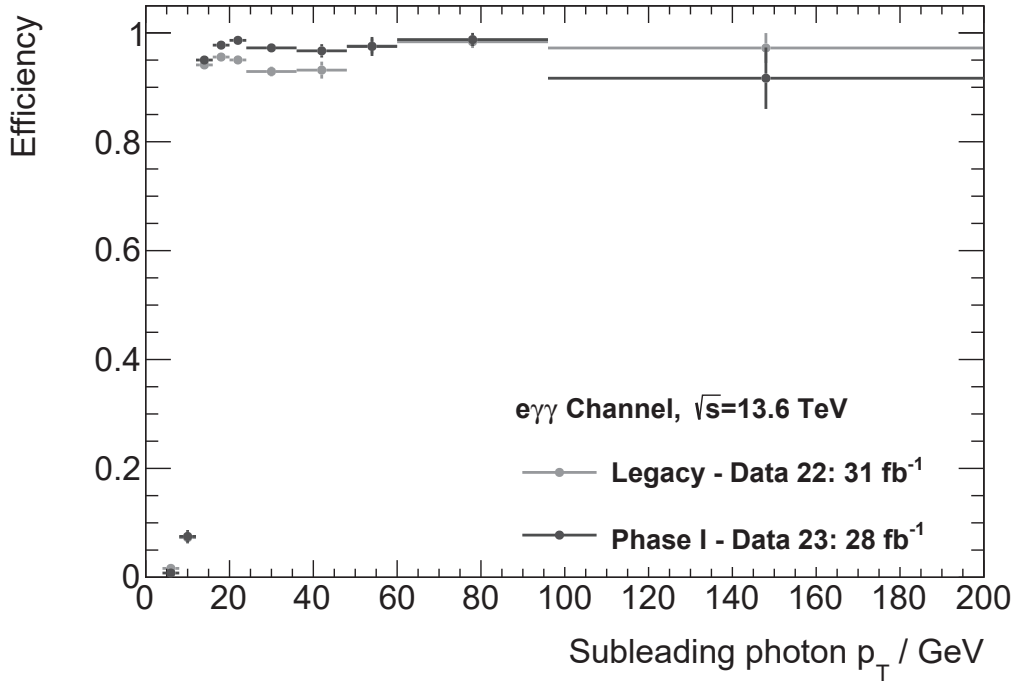

(a)

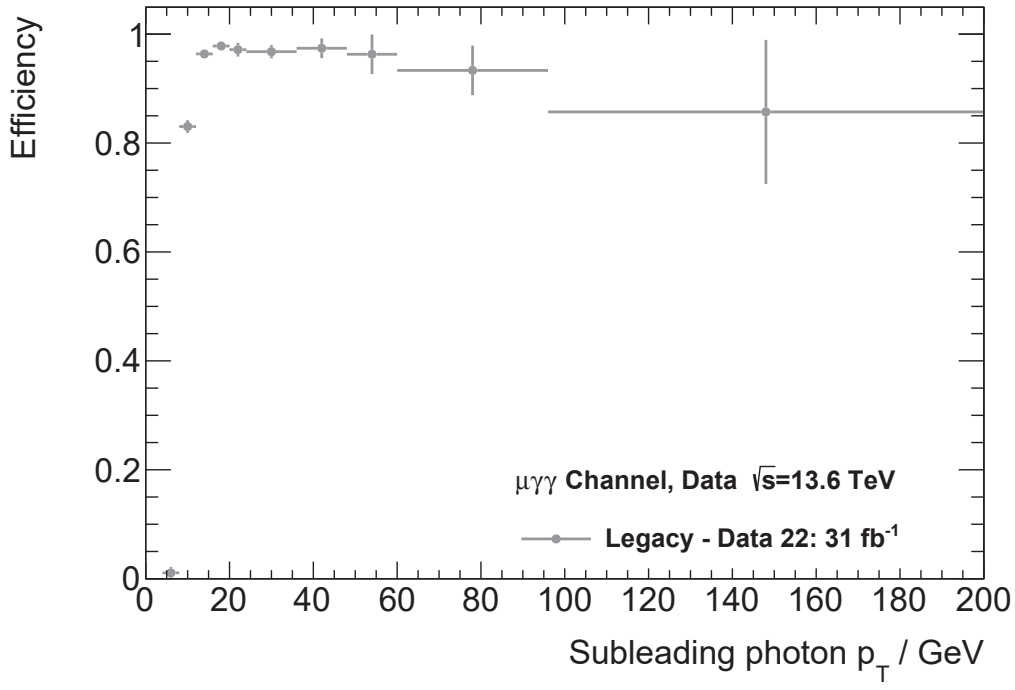

(b)

Figure 14: Results of the trigger matching efficiencies of the $l\gamma\gamma$ triggers. The results for both the Legacy and Phase-I systems for the $e\gamma\gamma$ trigger chain are shown in (a), while only the Legacy $\mu\gamma\gamma$ trigger results are shown in (b). The error bars represent the statistical uncertainties.

Therefore, the results show that these triggers are indeed a valid starting point for the $W\gamma\gamma$ analysis. Only the Phase-I $\mu\gamma\gamma$ has to be excluded from the analysis until the trigger matching algorithm is fixed accordingly.

7 $W\gamma\gamma$ Analysis

This section presents the results of the $W\gamma\gamma$ analysis in Run 3, with the W boson decaying leptonically either into an electron and electron-neutrino or muon and muon-neutrino. The final state consists of a high-p_T lepton, the presence of missing transverse energy coming from the neutrino and two isolated photons. This does not only include the production of the three EW bosons at tree level, but also other contributions such as FSR photons radiated off by the leptons as QED corrections (see Figure 15 (a)). The leptons considered here are only electrons and muons, leaving aside the tau decay of the W boson as part of the background.

This signal can be reproduced by other background processes. Therefore, the very first step is to take these backgrounds into account in order to suppress them accordingly by performing a dedicated event selection. The remaining contributions have to be estimated either by making use of MC simulations or by performing data-driven estimations.

The following section explains the background processes that must be taken into account. This is followed by the object and event selection that define the signal region (SR), which enhances the selection of $l\nu\gamma\gamma$ events and reduces the contributions from the backgrounds. The signal event estimation is also explained, including the comparison between different MC samples, as well as the estimation of part of the background. The section ends with a summary of the results obtained and the comparison to the Run 2 analysis as a validation.

7.1 Signal and Background Processes

Several background processes contribute to the signal produced by a lepton and two photons. Two types of background can be differentiated: promptly produced particles and fake or mis-identified contributions. In Figure 16, a diagram showing the contribution of the background processes is depicted, where the percentages are based on the Run 2 analysis results. These reflect how fake-dominated the $W\gamma\gamma$ analysis is.

Prompt Contributions

The first category can be estimated through MC simulations by applying the event selection and estimating the events that fall in the SR. First of all, WH with the Higgs decaying into two photons reproduces exactly the same final state as in $W\gamma\gamma$ (see Figure 15 (b)). For this reason it could be included as part of the signal, but it has not been estimated in this analysis. On the other hand, events where the W boson decays into a tau lepton could in principle be treated as signal as well. However, taus decay fast into electrons or muons, which are the leptons that most likely would be detected. Therefore, the tau channel is treated as background.

Among the other prompt contributions, the main background source is the triboson $Z\gamma\gamma$ production where one of the leptons coming from the Z boson does not pass

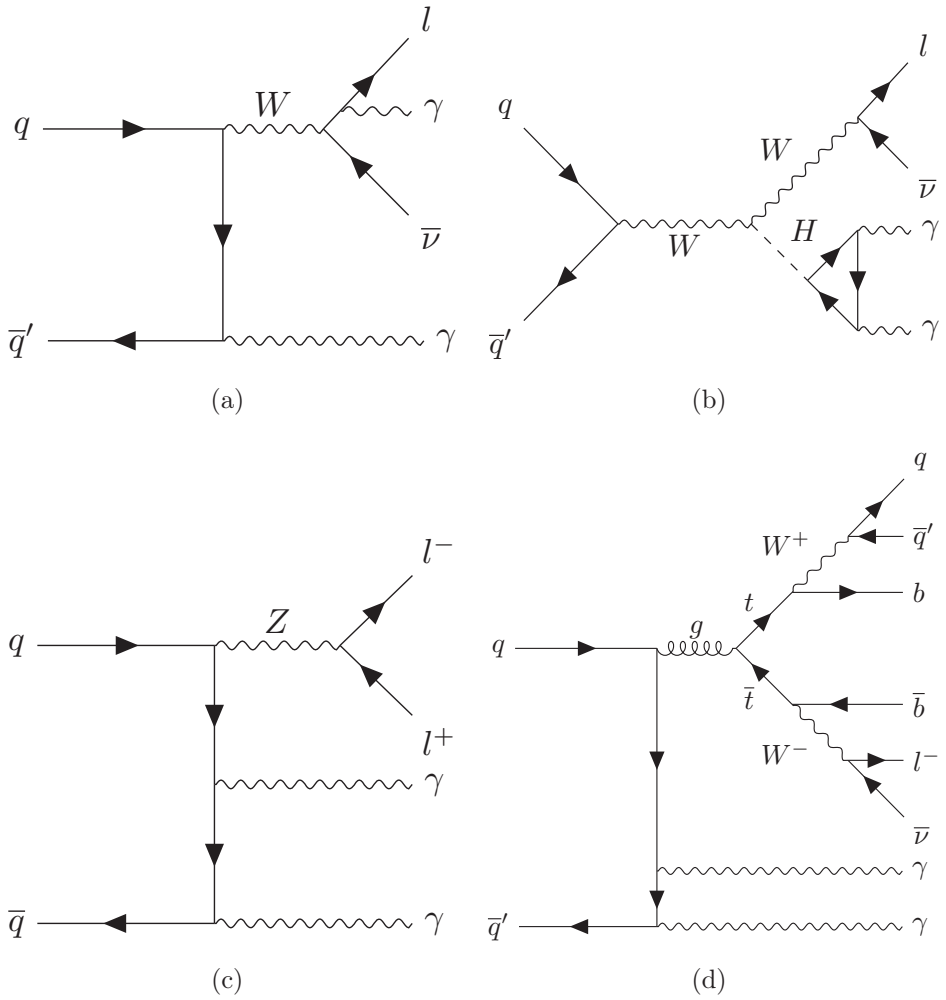

Figure 15: Feynman diagrams of processes with a lepton and two photons in the final state. In (a) the case of $W\gamma\gamma$ with one photon as FSR is shown, which is included in the signal event estimation in this thesis; in (b) the WH process with the decay $H \to \gamma\gamma$ is depicted; in (c) the $Z\gamma\gamma$ is shown, where it can be mistaken as signal when one of the leptons is not properly reconstructed; and in (d) the semileptonic $t\bar{t}\gamma\gamma$ process is shown.

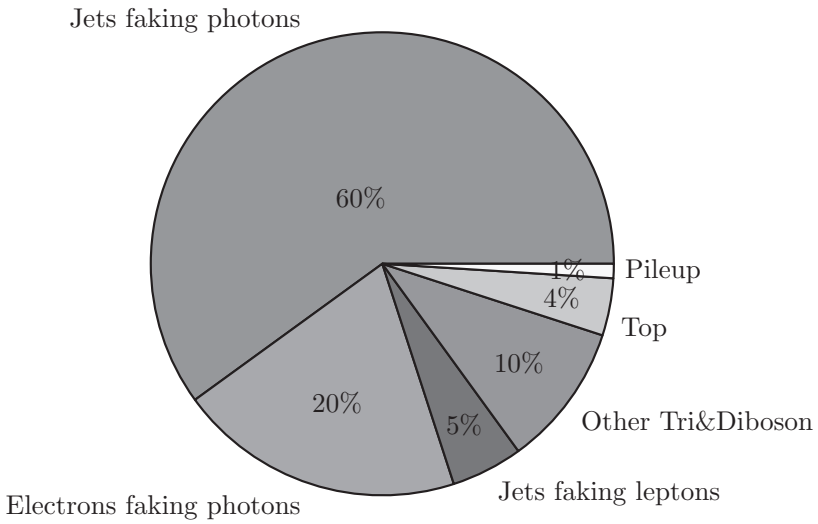

Figure 16: Pie chart of the backgrounds that reproduce the $W\gamma\gamma$ process. Values taken from the Run 2 results in [2].

the selection criteria. This process is shown in Figure 15 (c) and it is estimated in this analysis. These events, together with $WW\gamma$ and $W(\rightarrow \tau\nu)\gamma\gamma$ are included under "Other Di&Triboson" background in Figure 16. Other contributions to the background involve the top quark production, which include $t\bar{t}\gamma\gamma$, $tW\gamma\gamma$ and $tq\gamma\gamma$, where $t\bar{t}\gamma\gamma$ is the most relevant of the three and it is depicted in 15 (d).

Non-prompt Contributions

Among the non-prompt contributions, the main source of background comes from jets faking photons, mainly from $W(\gamma)$+jets events. The jets can decay into neutral mesons, such as pions, that successively decay into pairs of photons, which will be reconstructed as single photons if the meson has carried most of the jet momentum. These hadronic showers are not well modelled by MC simulations and even if isolation requirements reduce this contribution, it cannot be completely addressed. Therefore, data-driven methods are used in order to estimate this effect. Other non-prompt backgrounds also contribute and have to be estimated in a similar way. These include electrons faking photons, mainly from $Z\gamma$ with an additional FSR photon and jets faking leptons from Z boson production in association with jets. The fractions of these backgrounds are included in Figure 16, where they represent the dominant source of background. The last contribution are pile-up events, such as W boson and jets production can also overlap a diphoton event and contribute to the signal, which represent the smallest fraction of background.

It is important to notice that, despite not being well modelled in MC, some non-prompt contributions could be included in the MC estimations. In order to avoid double counting, this has to be taken into account accordingly in the data-driven methods studied.

7.2 Object and Event Selection

A collection of selection criteria at both particle and event level is defined in order to enhance the selection of $l\nu\gamma\gamma$ events and to reduce the background contributions[14]. Signal and background MC samples undergo the exact same selection. Regarding data, this is the case with the exception of the scale factors, which are not applied. These scale factors, provided by the Combined Performance groups in ATLAS, account for the differences between the MC simulations and the real recorded data, which involve different reconstruction effects.

Events are firstly selected using the three object triggers involving two photons with $p_T > 12\,\text{GeV}$ and an electron with $p_T > 24\,\text{GeV}$ or two photons with $p_T > 10\,\text{GeV}$ and a muon with $p_T > 20\,\text{GeV}$, as introduced in Section 6.1[15]. Moreover, the event is required to have a primary vertex.

Particle Level

The selection of the particles involved in the final state is broken down into different categories. These comprise objects which fulfil different criteria relevant for the intermediate stages of the event selection. A first *baseline* selection is done for photons and both a *preselect* and a *baseline* selection are performed for electrons and muons. Depending on the decay channel of the W boson, signal electrons or signal muons are selected and, in both cases, signal photons are selected, fulfilling always tighter criteria than the previous selection categories.

First of all, **baseline photons** are required to pass ambiguity and quality requirements, and the additional kinematic cuts of $p_T > 20\,\text{GeV}$ and pseudorapidity of $\eta < 2.37$, excluding the region $1.37{<}\eta{<}1.52$. **Signal photons** must pass the baseline selection and on top of that, the *tight* identification working point (WP) and the calorimeter-based isolation *Fixed-Cut Tight Calorimeter Only* WP, defined as $E_T^{\text{cone40}} < 0.022\,p_T + 2.45$ [GeV].

Preselect electrons must also satisfy ambiguity requirements and a pseudorapidity of $|\eta| < 2.47$, excluding $1.37{<}\eta{<}1.52$. They must additionally satisfy the *lhloose* identification WP, have a $p_T > 6\,\text{GeV}$ and pass the TTVA cut $|z_0{\cdot}\sin(\theta)| > 0.5\,\text{mm}$. **Baseline electrons** must pass the *lhmedium* identification WP and a $p_T > 25\,\text{GeV}$. Finally, the **signal electrons** must satisfy all the aforementioned cuts, plus fulfil the second TTVA cut $|d_0/\sigma_{d_0}| < 5$ and satisfy the variable-cone Tight isolation WP, *Tight_ VarRad*. The latter is defined in both calorimeter- and track-based variables as $E_T^{\text{cone20}}/p_T < 0.06$ and $p_T^{\text{varcone30}}/p_T < 0.06$ respectively.

For the muon channel, **preselect muons** are required to fulfil $|z_0 \cdot \sin(\theta)| > 0.5\,\text{mm}$, in order to satisfy that the track is coming from the primary vertex; satisfy the *medium*

[14]The criteria have been harmonised with the $W\gamma\gamma$ Run 2 analysis in order to facilitate their comparison.

[15]For simplicity, in MC only the Legacy triggers are used, since the efficiency with respect to Phase-I was shown to be similar. However, the MC results are all scaled to the full luminosity of the dataset where either the Legacy or the Phase-I trigger were used.

identification WP; and pass the kinematic cuts $p_T > 6\,\text{GeV}$ and $|\eta| < 2.4$. **Baseline muons** must have a $p_T > 25\,\text{GeV}$ and **signal muons** must fulfill the additional TTVA cut of $|d_0/\sigma_{d_0}| < 3$ and the pflow-based isolation *PflowTight_ VarRad* WP, defined by $E_T^{\text{pflow}} < 0.045$[16].

The scale factors applied on the photon and electron selection account for reconstruction, identification and isolation criteria. In the case of muons, identification and isolation scale factors are also applied, with additional TTVA scale factors.

Even though **jets** are not part of the final state of $W\gamma\gamma$, they are relevant for the overlap removal and the missing transverse energy calculation, both applied at event-level. For this reason, additional selection requirements have to be applied on these jets. They are required to fulfil $p_T > 20\,\text{GeV}$ and $|\eta| < 4.5$. A *Jet vertex tagger* (JVT) is applied in order to suppress pile-up contributions and thus only take into account jets originating from the primary vertex of the event. This is based on a neural network tagger, whose variable must pass the *tight* WP, covering jets with $20 < p_T < 60\,\text{GeV}$ and $|\eta| < 2.4$. The JVT has a scale factor associated which is also included.

Event Level

An overlap removal between the different types of objects needs to be applied. This selection step was explained in Section 6.3, and it is performed on baseline photons and jets and preselect electrons and muons, in the exact same way for both of the decay channels of the W boson.

Another step in the event selection is the reconstruction of the missing transverse energy, E_T^{miss}, since a neutrino is part of the final state. This is done by the `METMaker Tool` of the Athena framework after the reconstruction of photons, electrons, muons and jets, which includes an overlap removal step. The overall missing transverse energy is required to be $E_T^{\text{miss}} > 25\,\text{GeV}$. However, this reconstructed variable has a bad resolution at low transverse momenta. This is reflected by relative difference between the truth and reconstructed missing transverse energy, which is shown in Figure 17 for two bins in truth E_T^{miss} at low and high p_T, respectively.

After the baseline selection of photons and leptons and the overlap removal, trigger matching on the two leading photons and leading lepton is performed. In Figure 18, the comparison between baseline photons and electrons at both truth and reconstruction level prior to trigger matching are shown. Although a complete agreement is not expected between the two levels, the ratio in both of the distributions shows the absence of some scale factors coming from the object selection. The only scale factors missing are the three object trigger ones, which are expected to have an impact in the lower p_T regime, especially around the trigger thresholds. These scale factors could not be implemented due to some missing information in the corresponding `TrigGlobalEfficiencyCorrectionTool`, since it needs individual scale factors for

[16]The use of the pflow isolation represents a change with respect to the Run 2 analysis, which uses a similar definition as for the electron. As mentioned in Section 4.1, the use of this new variable is recommended now in offline analyses.

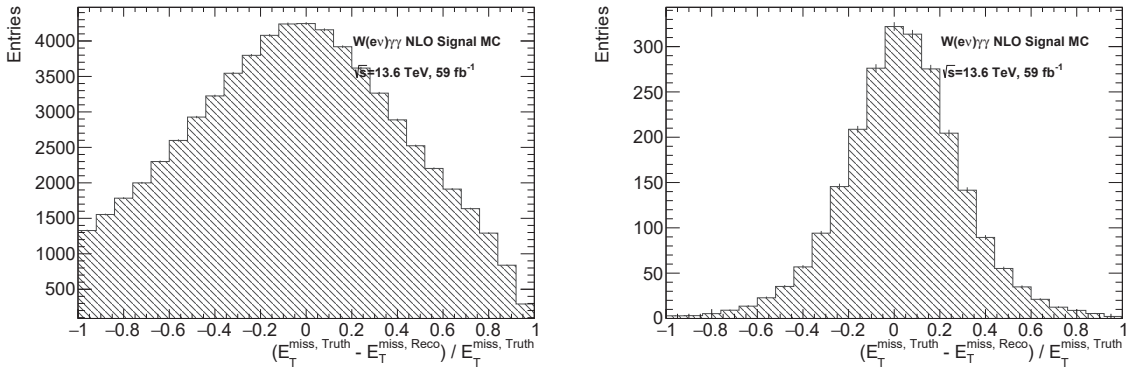

(a) (b)

Figure 17: Missing transverse energy resolution plots in bins of truth E_T^{miss}. In (a) the bin (20, 40) GeV is shown, while (b) corresponds to the bin (80, 120) GeV. The resolution in the remaining bins is shown in the Appendix E.

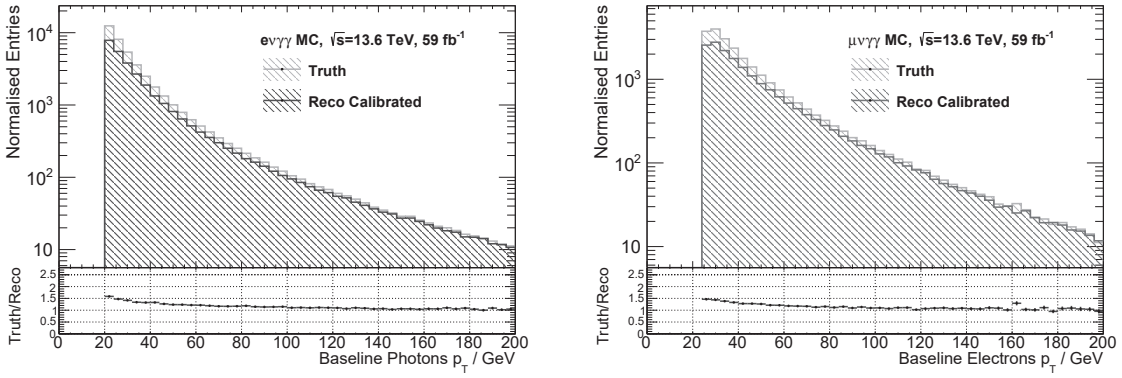

(a) (b)

Figure 18: Transverse momentum distributions of the baseline photons (a) and baseline electrons (b) at both truth and reconstruction level, for the signal electron channel MC.

each object and the photon part was not yet completed.

After trigger matching, the transverse mass of the W boson is calculated as follows:

$$m_T^W = \sqrt{2p_T^l E_T^{\text{miss}} (1 - \cos\Delta\phi)}, \tag{16}$$

where $\Delta\phi$ is the azimuthal angle difference between the lepton and the reconstructed E_T^{miss}. A cut on this variable is placed at $m_T^W > 40\,\text{GeV}$.

After these selection cuts, additional vetoes are applied at event level in order to reduce further background contributions. First of all, in order to reject events from processes involving Z and double W bosons, events with a same-flavour baseline lepton and an opposite-flavour signal lepton are rejected. The effect of the first cut becomes clear when comparing the $W\gamma\gamma$ and $Z\gamma\gamma$ event selection cutflow in the four MC samples shown in the following Section 7.5.

Particle Level	**Photons**		$p_T > 20$ GeV $\|\eta\| < 2.37$, exclude $1.37 < \|\eta\| < 1.52$ *tight* ID, *FixedCutTightCaloOnly* Iso $\Delta R_{\gamma,l/\gamma} > 0.4$
	Leptons	**Electrons**	$p_T > 25$ GeV $\|\eta\| < 2.47$, exclude $1.37 < \|\eta\| < 1.52$ *lhmedium* ID, *Tight_ VarRad* Iso $z_0 < 0.5$, $\|\sigma_{d_0}\| < 5$
		Muons	$p_T > 25$ GeV $\|\eta\| < 2.5$ *medium* ID, *PflowTight_ VarRad* Iso $z_0 < 0.5$, $\|\sigma_{d_0}\| < 3$
Event Level	**Combined**		Trigger matching on $l\gamma\gamma$ $E_T^{miss} > 25$ GeV, $m_T^W > 40$ GeV
	Leptons		No 2^{nd} preselect same-flavour lepton ($p_T > 6$ GeV) No opposite-flavour baseline lepton ($p_T > 25$ GeV)
	Vetoes		$Z(\gamma)$: $80 < m_{l\gamma(\gamma)}$ (GeV) < 100 b-jet: NNJvt on $p_T > 20$ GeV, $\|\eta\| < 2.5$, *tight* JVT

Table 4: Signal region definition.

In order to minimise further $Z\gamma(\gamma)$ contributions, another veto is defined: the $Z\gamma$-veto. It is explained in more detail in Section 7.4, when comparing the $Z\gamma$ and $Z\gamma\gamma$ background samples in the electron channel, but it is applied in both channels. Events must pass $p_T(l\gamma\gamma) > 30\,\text{GeV}$ and $m(l\gamma\gamma)$, $m(l\gamma_1)$ and $m(l\gamma_2)$ are excluded in the interval $[81, 100]\,\text{GeV}$, where γ_1 and γ_2 are the leading and subleading photons.

The last event level veto is the *b-jet* veto, which rejects jets containing b-flavoured hadrons, in order to reduce top-background contributions. Over the baseline jets, a multivariative classification algorithm is applied with a 77% efficiency for b-jets within $|\eta| < 2.5$. After this, events which contain at least one b-jet are rejected and the scale factors of its inefficiency are applied.

A summary of the $W\gamma\gamma$ signal region definition, including both particle level and event level requirements, is shown in Table 4.

7.3 Signal Estimation and Sample Comparison

In order to estimate the number of $W\gamma\gamma$ events, MC samples of $l\nu\gamma\gamma$ events in both electron and muon channel are needed. The W boson can be reconstructed from the lepton and the neutrino at truth level, or from the missing transverse energy at reconstruction level.

In the beginning of this thesis, no $l\nu\gamma\gamma$ MC sample was available for the Run 3 setup. For this reason, the request of a sample of NLO $e\nu\gamma\gamma$ events was initiated. This implied a local generation with MadGraph of the sample and the discussion of the validation of the sample with the responsible conveners of the electroweak sector within ATLAS. The resulting distributions of this validation process are included in

the Appendix B. The end goal was the production of the sample in PHYSLITE format, which was successfully produced. Additionally, two other samples became available, both Sherpa samples. The details of these samples are included in Section 5 Table 2.

For event estimation purposes, only the first centrally produced sample is used, since it is compatible with the other MC samples used and the datasets. However, the comparison with the other available samples is done in order to show the differences between MadGraph and Sherpa MC generators. The second interesting comparison between the signal MC samples are the two Sherpa samples. This serves as a validation of the reconstruction step performed with different releases of the Athena framework, as explained in Section 5. This is done for the sample of the W boson decaying in the electron channel, while in the muon channel only one Sherpa sample is studied.

Signal Samples Comparison in the Electron Channel

All of the samples contain $e\nu\gamma\gamma$ events with the W boson produced off-shell[17]. In Table 5 all of the generator cuts for the samples, i.e. the requirements on the objects included in the matrix element calculation, are summarised. These include cuts on the leading photons and on the topology of the event (ΔR cuts), among other criteria. The two Sherpa samples share the same selection at generation level, but the MadGraph sample has a different initial phase space. Another substantial difference between the MadGraph and Sherpa samples is that, while the Sherpa ones have similar statistics, the MadGraph one is more statistically limited. All the plots presented in this section are normalised accordingly to the corresponding cross section and sum of weights, as well as the Run 3 luminosity.

Sherpa 2.2.14	MadGraph5(3.5.4)_aMC@NLO + Pythia8 (with FxFx merging)
$p_T^\gamma > 7\,\text{GeV}$ $\Delta R_{\gamma,l} > 0.1$ $m_{l\nu} > 2\,\text{GeV}$ $\Delta R_{\gamma\gamma} > 0.2$ Frixione Isolation[18]: $R_{0\gamma} = 0.1$, $n = 2$, $\varepsilon_\gamma = 0.1$	$p_T^\gamma > 17\,\text{GeV}$ $p_T^{\text{jet}} > 8\,\text{GeV}$ No $\gamma \to e^- e^+$ Spliting Frixione Isolation: $R_{0\gamma} = 0.1$, $n = 2$, $\varepsilon_\gamma = 0.1$

Table 5: Generation level cuts for the signal samples. The Sherpa samples share the same settings.

Initial Distributions

When comparing the samples, the kinematic distributions of the events before harmonising the phase space, i.e. before applying the same selection cuts, give raise to quite different distributions. After the harmonisation, however, they are expected to agree within the uncertainties. A clear example of how the inital phase-space affects

[17] Off-shell production means that no constraints on the W boson are placed.

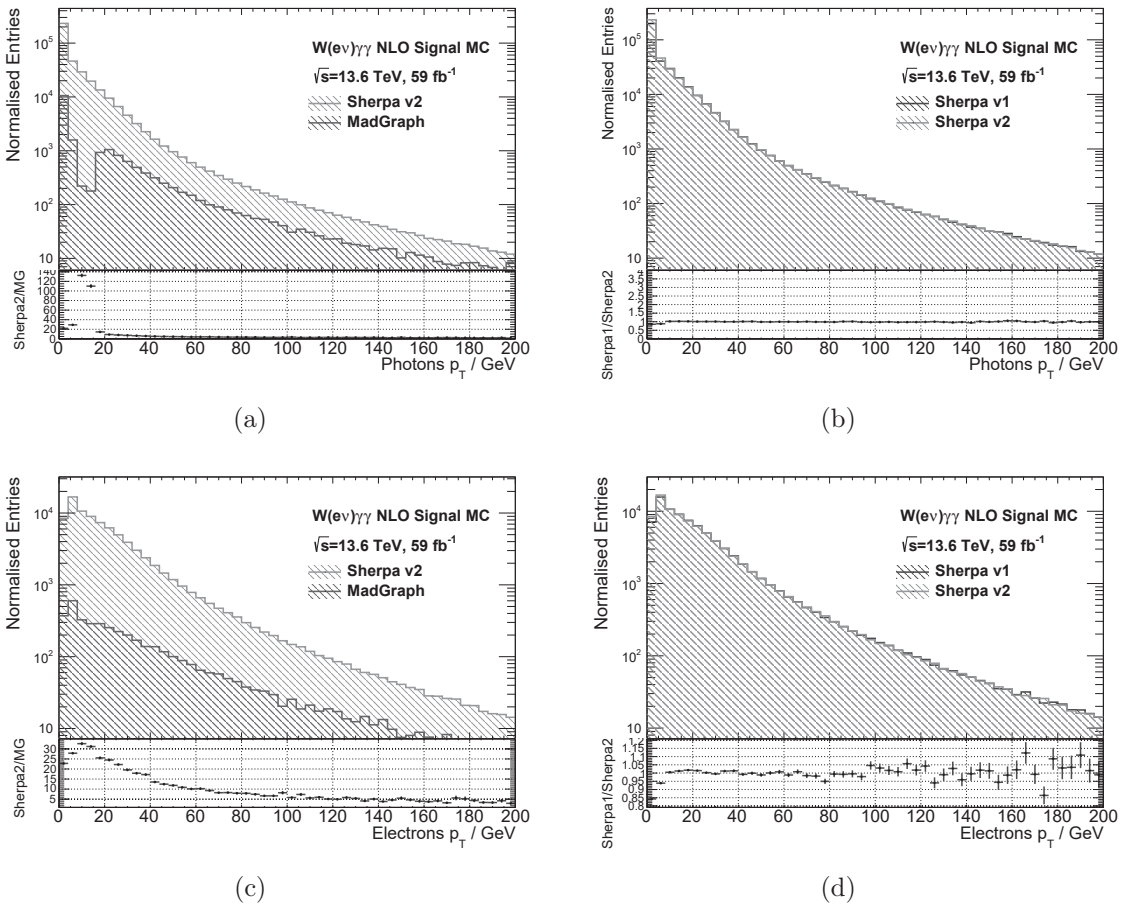

Figure 19: Transverse momentum distribution at reconstruction level of all photons and all electrons. In (a) and (c) the comparison between MadGraph and the second version of Sherpa and in (b) and (d) the comparison between the two Sherpa samples.

the comparison can be seen when taking a look at the transverse momentum distribution of all reconstructed photons in the sample at reconstruction level. This is shown in Figure 19 (a), where the Sherpa samples have a subtle peak from 7 GeV on, while the MadGraph sample has the peak from 17 GeV on, reflecting the cuts at generation level on the photon p_T. In Figure 19 (c), the comparison between the same samples for the electron transverse momentum is shown, where the difference in the topological conditions of the electron could play a role in the discrepancies.

When these initial distributions of the photons and electrons are compared between the two Sherpa samples, shown in Figures 19 (b) and (d) respectively, a better agreement can already be seen, with a ratio that differs by 5% within the statistical uncertainties. However, an increase of low-p_T photons and electrons in the second Sherpa sample is noticeable, shown as a well in the ratio below 10 GeV. These low-p_T contributions do not contribute to the signal selection, since they would be cut out by the p_T selection. However, they could still have an impact on the missing transverse energy calculation.

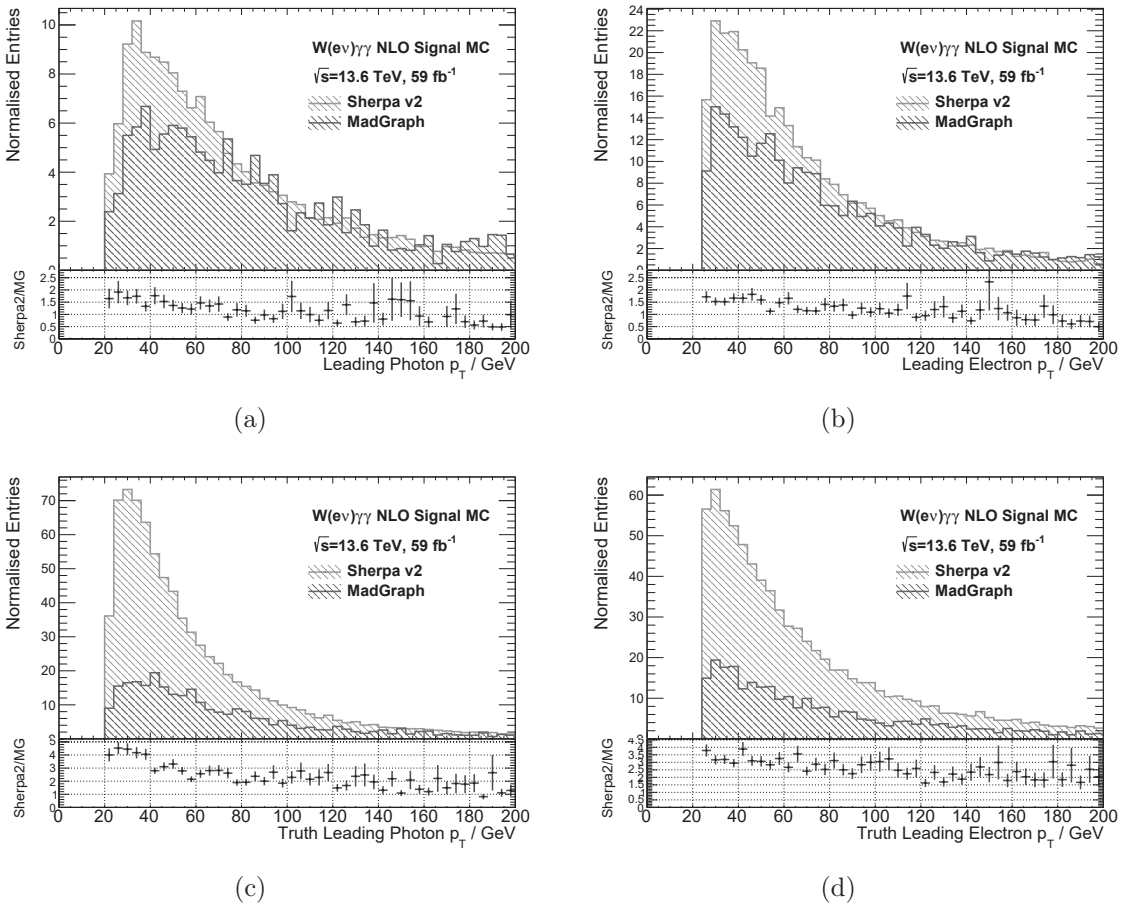

Figure 20: Transverse momentum distributions at reconstruction level of leading photons (a), subleading photons (b) and leading electrons (c); and relative distance between the leading photons and leading electrons (d), subleading photons and leading electrons (e) and leading and subleading photons (f). All of them show the comparison between the MadGraph and the second version of the Sherpa sample.

Leading Particles Distributions

The MadGraph and Sherpa samples are expected to agree within certain range once the signal selection criteria have been applied, since this should compensate for any previous cuts with lower thresholds. In Figures 20 (a) and (b), the final leading photons and electrons p_t distributions are shown. However, it can be seen that there is not a clear agreement when looking at the ratio of the plots. In order to understand the origin of this disagreement, the truth distributions are also compared (see Figures 20 (c) and (d)). The great discrepancies at this level reveal an issue either at generation level or a flaw in the harmonisation of the phase space, which is in any case not understood. Further comparison at truth level between other variables would be necessary in order to discern the source of this difference, which was not possible within the time frame of this thesis.

When looking at the same distributions comparing the two Sherpa samples, shown

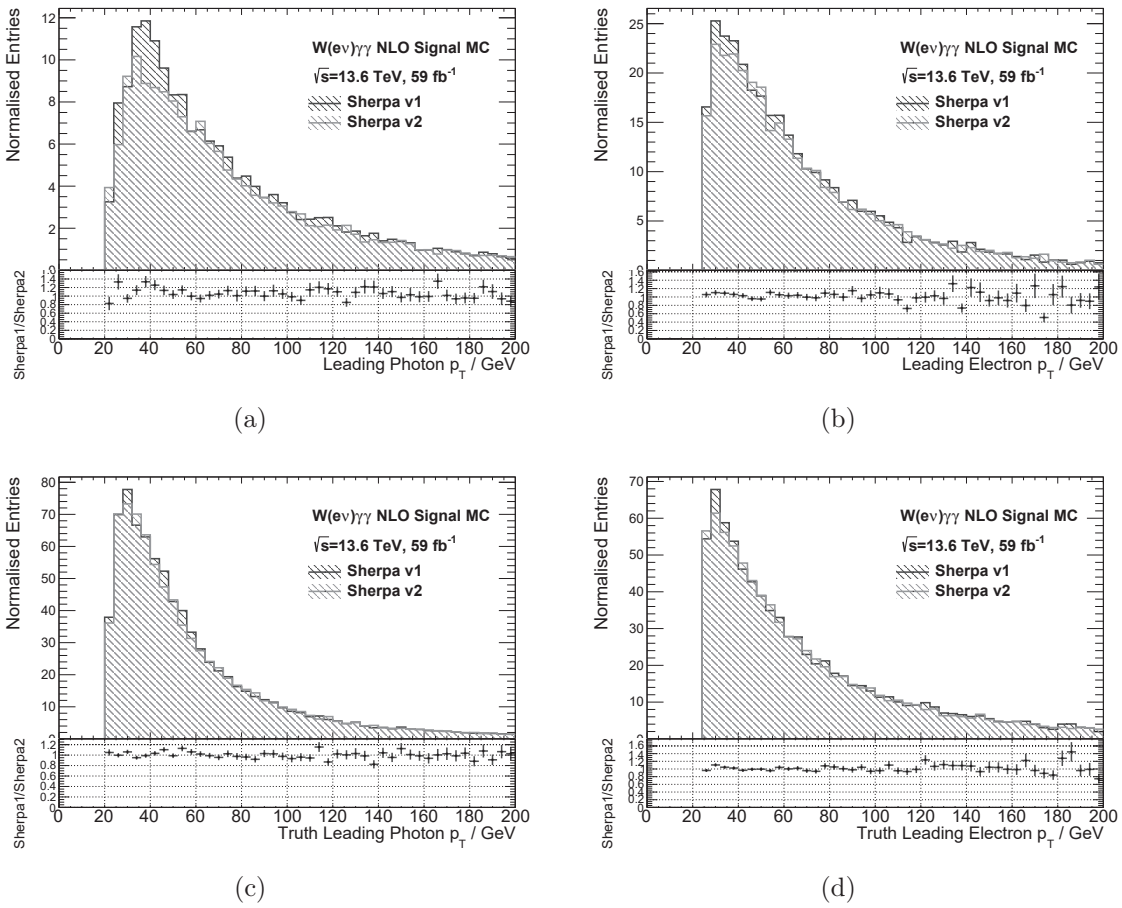

Figure 21: Transverse momentum distributions at reconstruction level of leading photons (a), subleading photons (b) and leading electrons (c); and relative distance between the leading photons and leading electrons (d), subleading photons and leading electrons (e) and leading and subleading photons (f). All of them show the comparison between the two Sherpa samples.

in Figures 21 (a)-(d), a better agreement can be seen with respect to the previous comparison. However, in the case of the leading photons and electrons, (a) and (b), the difference reaches up to 40% in the lower p_T regime in the photon distribution. The deviations in the end tails are nevertheless expected due to the statistical fluctuations in the high-p_T regime. The leading electrons distributions show a better agreement in the low-p_T regime. In addition, when comparing the same distributions at truth level, a better agreement is found in both distributions.

The discrepancies between the two Sherpa samples reflect the impact of the reconstruction step on the sample production. Further dive into the reconstruction changes from one Athena release to another would be needed in order to understand the discrepancies. However, this is beyond the scope of this thesis.

W Boson Kinematics

The full reconstruction of the W boson mass has been and still is a challenge in the particle physics field, which combining the precise measurements of LEP, D0, ATLAS and LHCb experiments yields a value of $m_W = 80369.2 \pm 13.3\,\text{MeV}$ [67]. This is due to the fact that the neutrino cannot be detected and the missing transverse energy is exploited instead. Additionally, since at truth level the neutrino information is available, the transverse mass m_T^W distributions at both truth and reconstruction level can be studied.

It can be seen in both of the truth m_T^W, in Figures 22 (a) and (b), where the different and same generator comparison are shown respectively, that the distributions present a peak at around m_W. This peak is know as the *Jacobian Peak* and it is present when the W boson is studied in the rest frame. Adding detector effects at reconstruction level introduces an smearing effect, shown in Figures 22 (c) and (d), where the tail after m_W arises. The comparison between the different generators samples reflects that in the case of the MadGraph sample the peak in the reconstructed m_T^W is less prominent than in the Sherpa samples. Once again, this constitutes an effect that is not well understood.

Another interesting variable to look at is the charge of the W boson. More positively-charge bosons are expected since the initial pp collisions involve positively-charged particles, and this effect can be seen in Figures 22 (e) and (f).

Event Expectation Comparison

The event estimation along with the statistical uncertainties of the three signal samples for the Run 3 luminosity is shown in the following table:

Sherpa version 1 (24.0.12)	**MadGraph**	**Sherpa version 2 (24.0.21)**
92.54 ± 1.99	79.32 ± 3.59	83.46 ± 1.35

Table 6: Event expectation results of the three signal electron channel MC samples compared.

The resulting distributions were not in agreement. Especially, in the case of the different generators comparison (second version of Sherpa and MadGraph). However, between the two comparable samples, i.e. same sample production settings, the MadGraph and the second version of the Sherpa sample event estimations are in agreement within the uncertainties. The statistical difference between the samples is shown in the uncertainties, which are solely statistical. When taking a look at the cutflow diagram of the event selection comparing the three samples, shown in Figure 23, it can be seen how the discrepancies in the number of events are compensated as the event selection criteria are applied.

Several conclusions can be drawn from these results. From comparing different gen-

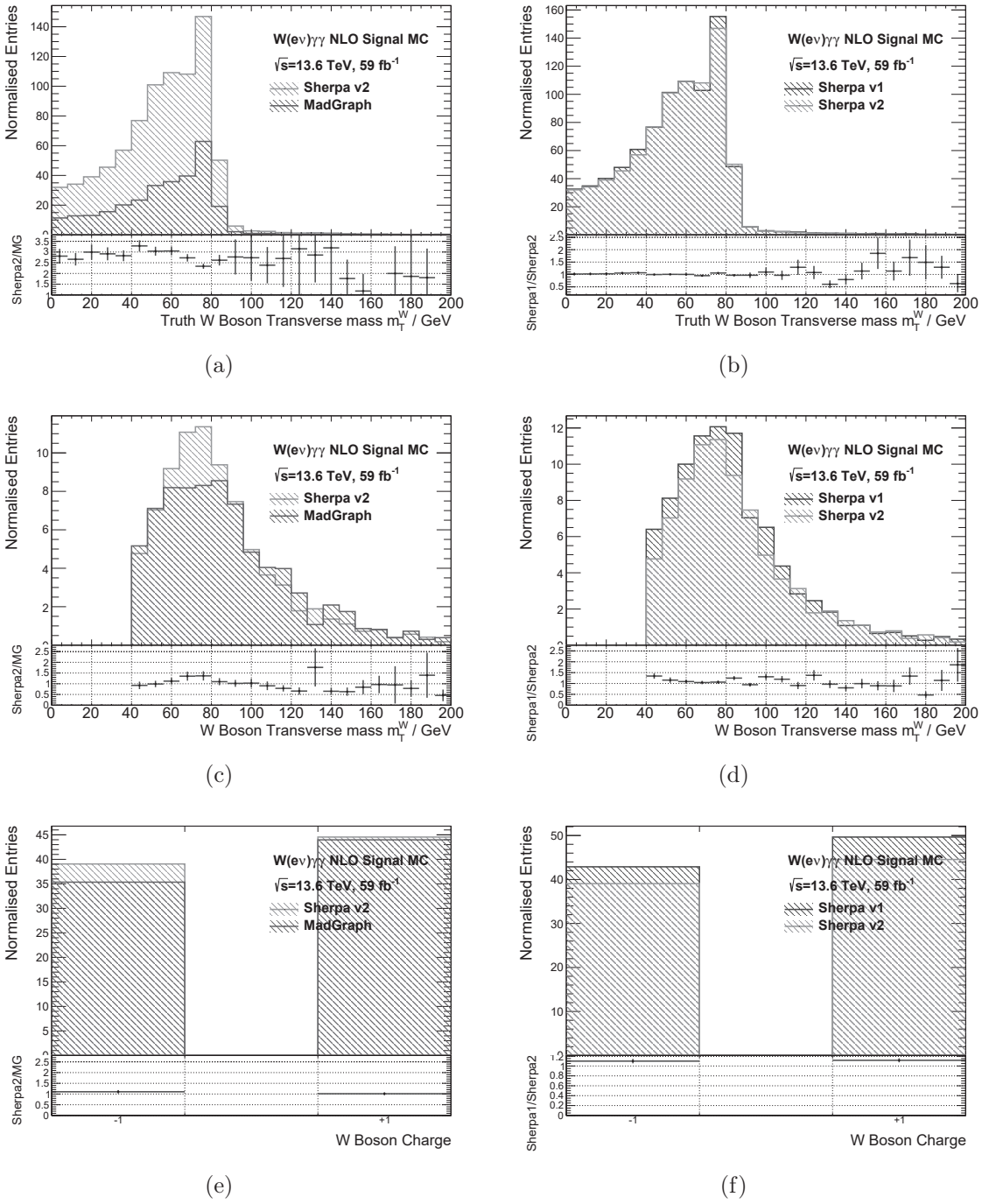

Figure 22: Transverse mass distribution at truth and reconstructed level adter the SR criteria were applied and the charge of the final W boson. In (a), (c) and (e) the comparison between MadGraph and the second version of Sherpa is presented and in (b), (d) and (f) the comparison between the two Sherpa samples is shown.

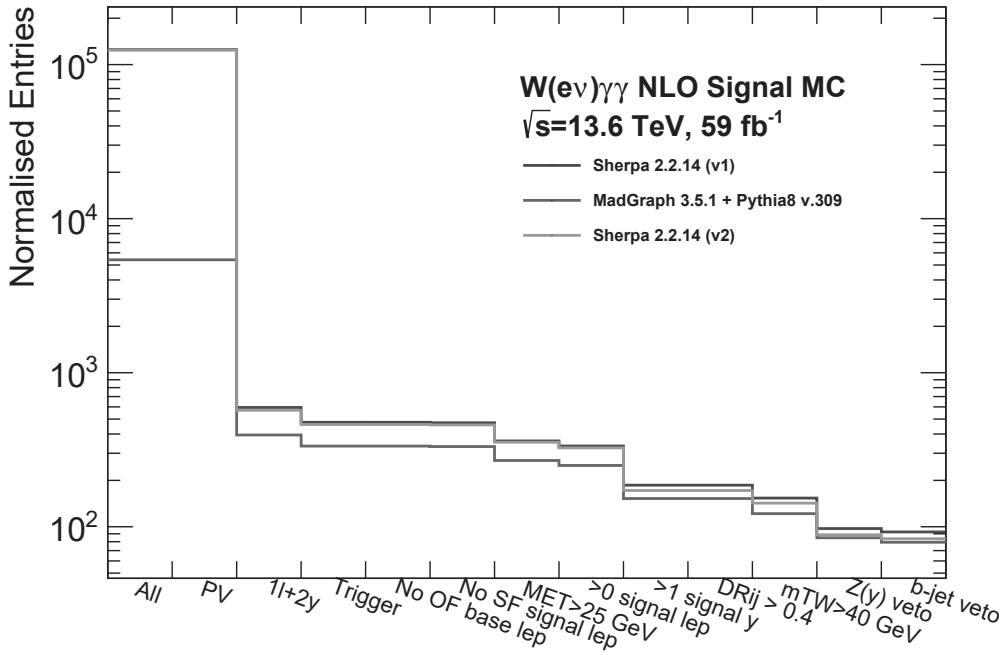

Figure 23: Cutflow diagram of the event selection on the three signal electron channel MC samples.

erator samples, but same reconstruction framework release, it was seen that a deeper study of the distributions and the topology of the particles involved is needed in order to understand where the discrepancies arise from. The time limitation of this thesis prevented from the extension of these studies.

In the case of the same generator, but different reconstruction framework release, differences were still shown in the distributions. This reflects the need of comparing samples which were produced under compatible settings. Using the latest releases of the Athena framework can bring significant differences, which have not yet been validated or addressed. When specific settings differ from one sample to another, further validation comparisons are needed.

7.4 Background Estimation

Out of all of the background which contribute to the $W\gamma\gamma$ estimation, the $Z\gamma$ and $Z\gamma\gamma$ processes were studied. Additionally, the contribution of $W(\tau\nu)\gamma\gamma$ events was estimated.

$Z\gamma(\gamma)$ and the $Z\gamma$ veto

In the case of $Z\gamma\gamma$, the particles reproducing the signal are all prompt and can be estimated properly though MC simulations. However, in the case of the diboson $Z\gamma$,

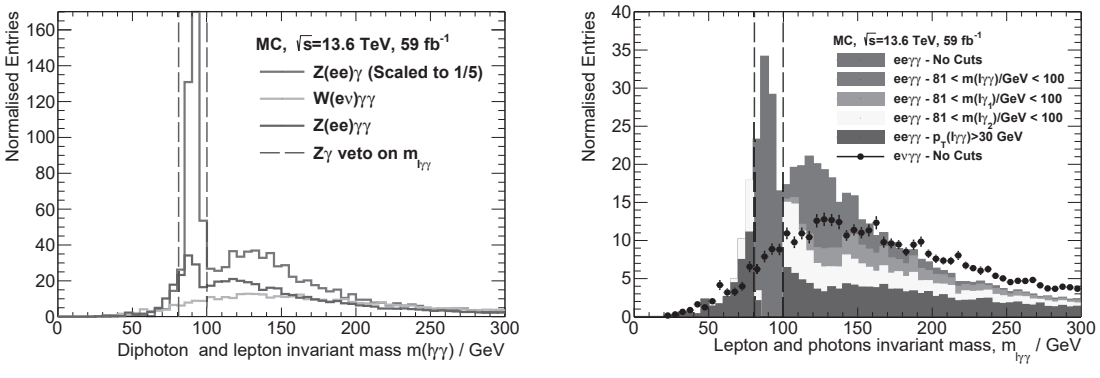

(a) (b)

Figure 24: Distributions of the invariant mass involving the two photons and the electron, $m_{l\gamma\gamma}$. In (a), the distribution before any $Z\gamma$ veto cut is shown for the samples $W\gamma\gamma$, $Z\gamma\gamma$ and $Z\gamma$, where the latter is scaled for a better visualisation. In (b), the effect of each cut on the $m_{l\gamma\gamma}$ variable is shown for the $Z\gamma\gamma$ events.

the contribution is mainly non-prompt[19]. The non-prompt contribution includes the case where one lepton coming from the Z boson is reconstructed and the other one is mis-reconstructed as a photon, which would fall into the fraction of background of electrons faking photons. This was shown in Figure 16 that comprises the second main background contribution. This fake contribution cannot be estimated through MC, since these contributions are not well modelled, and a data-driven method would have to be used. A veto dedicated to reduce these two contributions was briefly introduced in Section 7.2 and explained now in more detail.

In contrast with processes involving the W boson, where the neutrino is poorly reconstructed through the missing transverse energy in the event, events with Z bosons can be well constrained since both of the leptons can be actually detected. Therefore, exploiting the invariant mass of the Z boson can help to discern the $Z\gamma(\gamma)$ contributions.

In the $Z\gamma$ process, the main contribution comes from one of the leptons (mainly electrons) being mis-reconstructed as photons. Taking this into account, when studying variables such as the invariant masses involving the prompt electron and photon and fake photon, a peak is expected to appear around the Z boson mass, $m_Z = 91.187\,\text{GeV}$ [68].

Following the strategy performed in the Run 1 [28] and Run 2 analyses [2] of the $W\gamma\gamma$ Analysis, a set of constraints are placed in four variables: $p_T(l\gamma\gamma)$, $m(l\gamma\gamma)$, $m(l\gamma_1)$ and $m(l\gamma_2)$, where γ_1 and γ_2 are the leading and subleading photons respectively. In the case of the invariant mass variables, a peak around m_Z represents a different physical process of the event in $Z\gamma(\gamma)$:

- If $m(l\gamma\gamma) \sim m_Z$: in $Z\gamma\gamma$ both of the photons have been produced as FSR and in $Z\gamma$ one photon was FSR plus an electron faked a photon.

[19]From $Z\gamma$, also a photon could be produced as FSR, which would be included in the $Z\gamma\gamma$ contribution. This introduces overlaps between samples that would have to be taken into account.

- If $m(l\gamma_1) \sim m_Z$: in $Z\gamma\gamma$ the leading photon was produced as FSR and in $Z\gamma$, the leading photon is the electron fake.
- If $m(l\gamma_2) \sim m_Z$: in $Z\gamma\gamma$ the subleading photon was produced as FSR and in $Z\gamma$ the subleading photon is the electron fake.

In addition to these cases, $Z\gamma\gamma$ events could have as well one of the electrons faking a photon.

In order to visualise these effects, the distributions of the signal and $Z\gamma(\gamma)$ processes are compared. An example of the variable $m(l\gamma\gamma)$ reconstructed from baseline and triggered leading objects in the three samples is shown in Figure 24 (a). Since $Z\gamma$ process has a significantly higher cross section with respect to the other two triple boson processes, the $Z\gamma$ events are scaled in order to compare the shapes of the distributions. The difference in the cross section also explains the considerable contribution of the electron fakes that is expected (previously shown in Figure 16).

Taking the Run 2 optimised values of the veto cuts, events must pass $p_T(l\gamma\gamma) > 30\,\text{GeV}$ and $m(l\gamma\gamma)$, $m(l\gamma_1)$ and $m(l\gamma_2)$ are excluded in the interval $[81, 100]\,\text{GeV}$. In Figure 24 (b), the effect on $m(l\gamma\gamma)$ is shown. Here, only the $Z\gamma\gamma$ is included in comparison to $W\gamma\gamma$, in order to picture the effect of the other cuts in this particular variable.

When comparing the rejection of events at the $Z\gamma$ veto step on both $W\gamma\gamma$ and $Z\gamma\gamma$ events, for both electron and muon channel, the desirable effect on this background is obtained: the $Z\gamma\gamma$ events are reduced a 68.7%, while $W\gamma\gamma$ are reduced a 18.4%.

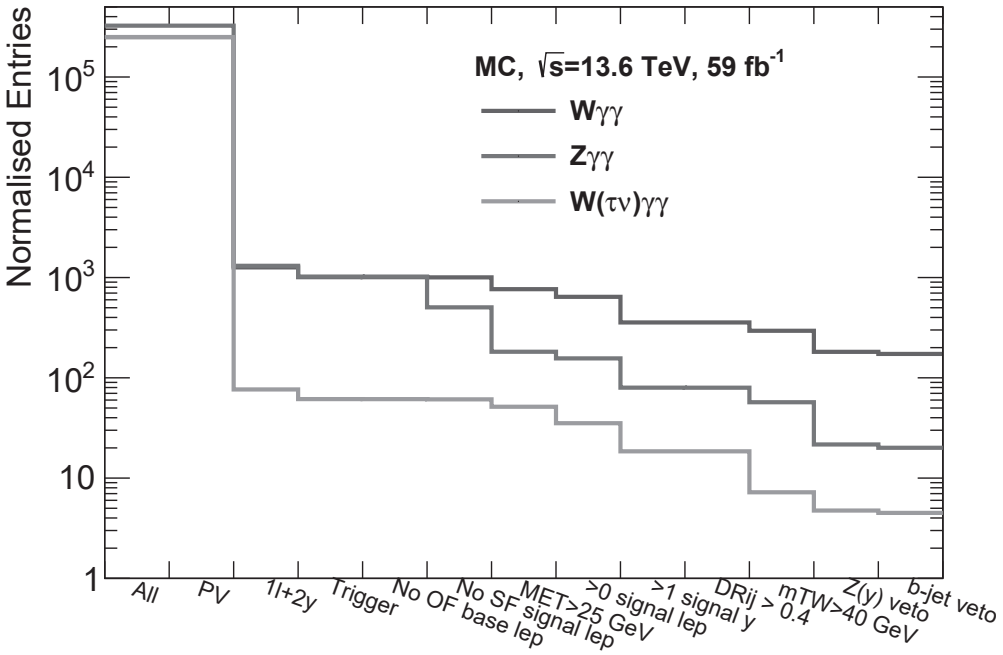

Figure 25: Cutflow diagram of the event selection on the combined channels of the signal and background MC samples.

7.5 Results

The combined results on the signal and background MC samples studied are shown in Figure 25 for the different event selection criteria, yielding the following number of events:

Process	Expected events	Total expected events
$W(e\nu)\gamma\gamma$	92.54±2.00	173.07±2.57
$W(\mu\nu)\gamma\gamma$	80.53±1.61	
$Z(ee)\gamma\gamma$	11.56±0.55	22.37±0.77
$Z(\mu\mu)\gamma\gamma$	10.81±0.54	
$W(\tau\nu)\gamma\gamma$	4.49±0.42	4.49±0.42

Table 7: Event estimation results for each MC sample separated by channel and combined.

Additionally, the total number of events was measured in data, yielding the following values:

Process	Data 22	Data23
$W(e\nu)\gamma\gamma$	151±12	154±12
$W(\mu\nu)\gamma\gamma$	101±10	-
Total	252±16	154±12

Table 8: Results per channel and combined of the events that pass the SR criteria in data.

These results include all the background and signal contributions that pass the selection criteria of the SR. However, due to the fact that the Phase-I $\mu\gamma\gamma$ trigger matching was not possible to perform, the event estimation for data of 2023 is not included. However, the trigger information is present in the datasets and, once the problem with the trigger matching tool is solved, an estimation of the events in the first two years of Run 3 will be possible.

Comparison to Run 2

In order to understand if the MC-estimated events are reasonable, a comparison to the previous analysis in Run 2 can be made. For Run 3, the centre-of-mass energy of the *pp* collisions rose from 13 TeV to 13.6 TeV, i.e. around a 4.6% increase. This also translates in a higher expected cross section and therefore, for the same luminosity, a higher number of expected events. Since the luminosity available so far in Run 3 does not reach the levels of Run 2, a comparison with the Run 2 luminosity can be done by scaling the number of events to that value, by changing the value of L_{int} in Equation 13. The comparative results are shown in Table 9.

It is shown that there is an increase of 4% in the case of the signal MC, in agreement to what was expected. The increase is smaller in the case of the $Z\gamma\gamma$ background and

Process	Run 2 Events	Run 3 Events	Ratio (Run3/Run2)
$W\gamma\gamma$	390.4±21.4	406.36±6.03	1.04
$Z\gamma\gamma$	52.1±13.3	52.52±1.81	1.01
$W(\tau\nu)\gamma\gamma$	10.8±1.8	10.54±0.98	0.98

Table 9: Comparison between Run 2 and Run 3 events for the different processes, both scaled to Run 2 luminosity ($L_{int} = 139\,\text{fb}^{-1}$). The values of Run 2 are taken from [2] and the uncertainties shown are systematic and statistical. The uncertainties in the Run 3 results are only statistical.

	Run 3 (Data 2022)	Run 2	Ratio (Run3/Run2)
L_{int} /fb^{-1}	31	140	0.22
Events	252	1136	0.22

Table 10: Comparison between Run 2 and Run 3 events measured in data from 2022. The event measurement from Run 2 is taken from [2].

$W(\tau\nu)\gamma\gamma$ shows a decrease of 2%. These differences are not in any case concluding due to the high uncertainties on the Run 2 estimations. Several effects which are not quantified could play a role in this estimation, such as the absence of some scaling factors, the change in isolation definitions (in the case of the muon) or the lack of systematic uncertainties.

In addition, a comparison with Run 2 can be carried out for the events measured in data. The difference in luminosity from Run 2 to Run 3 should be comparable to the difference in events. Taking the events measured in data from 2022 and leaving aside the incomplete measurement in data from 2023 (shown in Table 8), this comparison between Run 2 and Run 3 is shown in Table 10. The agreement in the ratios obtained reflect the consistency in the event selection between the two analyses.

Uncertainties

All of the uncertainties provided along with the results are exclusively statistical. However, systematic uncertainties are expected to have an impact since they come from many sources.

First of all, the estimation of both signal and background MC should include several sources of experimental uncertainties coming from the event reconstruction. Regarding electrons and photons combined, they are affected by scale and resolution uncertainties in the joint algorithm reconstruction. They are also affected respectively by the different reconstruction, identification, isolation and trigger efficiencies. In the case of muons, the uncertainties associated come from reconstruction, track-to-vertex associa-

tion performance, isolation and trigger efficiencies. Jets are also affected by scale and energy resolution uncertainties and the jet flavour tagging contributes with its efficiency. In addition, the reconstruction of the missing transverse energy is also expected to be heavily affected by the resolution, which is shown not have a good agreement between the truth and reconstruction information in the samples (see Appendix E).

The MC samples are also affected by theoretical uncertainties coming from the event generation. These include the QCD corrections, such as the uncertainties in the cross section calculation and the missing higher order terms, the different parton distribution function variations and the uncertainty of the strong coupling constant. The second contribution can be visualised as error bands in the validation plots for the signal sample requested in Appendix B.

8 Summary

Out of all the possible ways of looking for new physics, the Electroweak sector offers an interesting path. Precision measurements on weak gauge boson self-interactions could give raise to anomalies that go beyond the SM. In particular, triple and quartic gauge couplings of the $W\gamma\gamma$ process are predicted by the SM and high-energy measurements are needed in order to gain more sensitivity within the frame of effective field theories, where deviations on the couplings can be estimated.

The analysis presented here consists on a first look into the $W\gamma\gamma$ process using the data recorded by the ATLAS detector in the ongoing Run 3 data-taking period of the LHC. The leptonic decays of the W boson into either an electon or a muon are considered. This process has already been measured using Run 2 data, but now a higher centre-of-mass energy, $\sqrt{s} = 13.6\,\text{TeV}$, is used and, by the end of the Run 3, a higher luminosity will become available. This translates into a higher cross section of the process and therefore, more expected events. So far, the data recorded in the first two years is analysed, corresponding to an integrated luminosity of $59\,\text{fb}^{-1}$.

The Run 3 in ATLAS involves several detector upgrades and changes within the baseline framework of the ATLAS experiment, Athena. Furthermore, a new analysis format was introduced, PHYSLITE, and it is intended to replace the old derivation formats in the following upcoming years, since they consist on a more efficient way of storing the information that the ATLAS experiment provides. This format is exclusively used in this analysis.

Among the changes at detector level for the new run, a new trigger system was installed and commissioned. This thesis studies the changes relevant for the $W\gamma\gamma$ analysis. It focuses on the performance of three-object triggers involving a lepton and two photons. The new Phase-I trigger system is compared to the previous Legacy system. In both lepton channels, the triggers show a similar performance and reach efficiencies above 90%. Additionally, the trigger matching performance of the triggers is also compared. The $e\gamma\gamma$ triggers show a similar performance and reach efficiencies of about 85% for both systems. On the other hand, the legacy $\mu\gamma\gamma$ trigger has an efficiency over 80%. The Phase-I $\mu\gamma\gamma$ trigger could not be tested, due to a problem in a framework tool that has been reported to the responsible developers. However, these triggers are shown to be working properly otherwise.

The analysis of the $W\gamma\gamma$ process includes the definition of the background sources that can mimic the same final state. The event selection criteria that enrich $l\nu\gamma\gamma$ events are explained, followed by the signal and two background MC estimations.

A total of three samples are studied for the signal event estimation in the electron channel of the W boson decay. The comparison of two samples produced with different MC generators, Sherpa and MadGraph, is shown. One of the samples was validated and requested (MadGraph), while the other one was requested by another analysis group (Sherpa). The discrepancies that are shown between the samples are not understood and the time limitation of the thesis did not allow further investigation. Although the distributions do not show agreement, the event estimation does is consistent within the

uncertainties. Additionally, two samples produced with the same generator (Sherpa), but different reconstruction framework releases, are compared. Here, neither the kinematic distributions, although with less discrepancy than the previous comparison, nor the event estimation are in agreement. This shows the importance of the use of compatible reconstruction framework releases for all samples. This framework is constantly being upgraded and using the latest versions can bring discrepancies that have not been validated or addressed yet.

The $W\gamma\gamma$ event expectation for the first two years of the Run 3 is presented as 173.1 ± 2.6 events. In order to validate this estimation, a scaling to Run 2 luminosity is performed comparing the events obtained here with those from the Run 2 analysis. This shows an increase of 4%, which reasonably accounts for the increase of centre-of-mass energy from one data-taking period to the next, as well as improvements in the detector and particle identification frameworks. Additionally, measurements in data show a consistent result with respect to the Run 2 analysis.

A Trigger Performance Studies Distributions for the Muon Channel

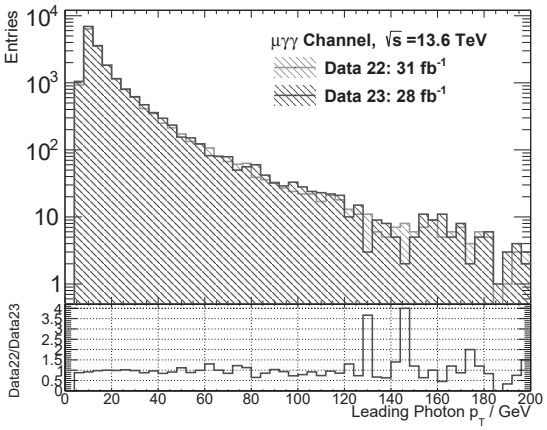

(a)

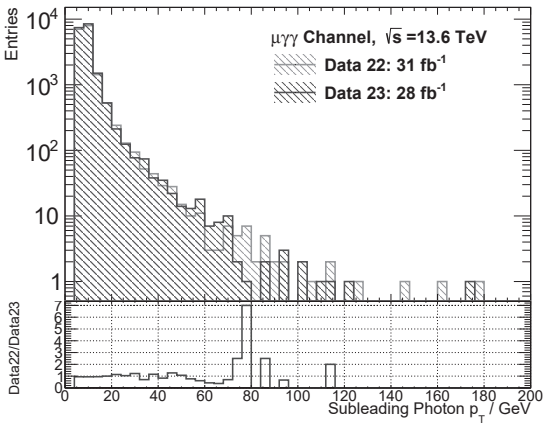

(b)

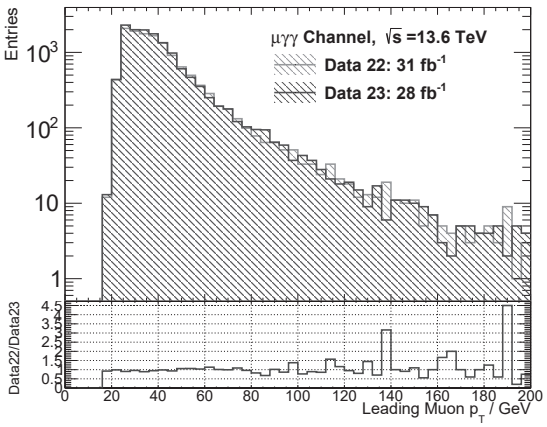

(c)

Figure 26: Transverse momentum distributions of the leading photons (a), subleading photons (b) and leading lepton (c) for the muon channel.

B Signal Electron Channel MC Sample Validation

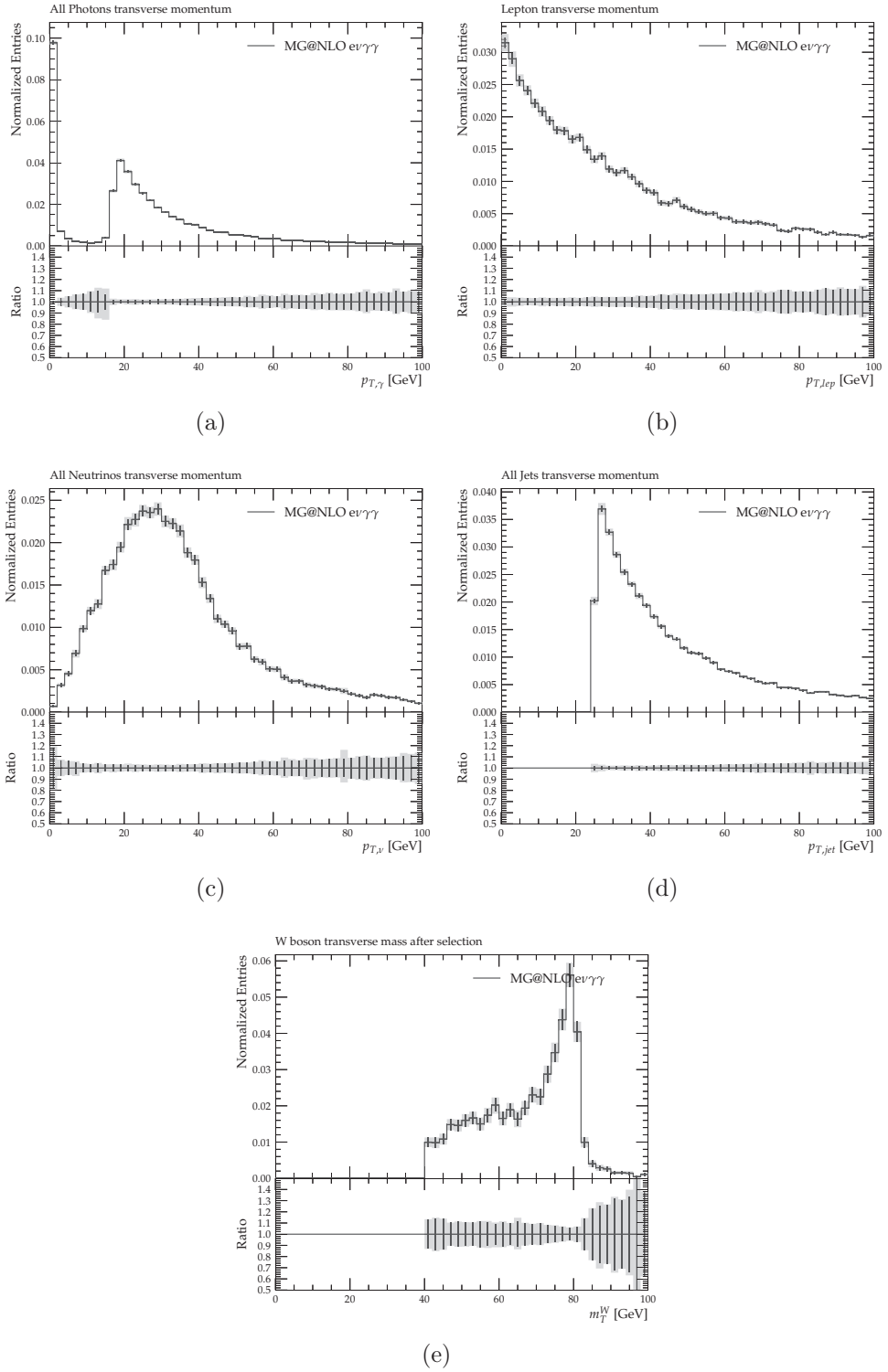

Figure 27: MadGraph $e\nu\gamma\gamma$ MC sample validation plots, including the transverse momentum of photons (a), leptons (b), neutrinos (c) and jets (d); and the transverse mass of the W boson.

C Signal Electron Channel MC Results

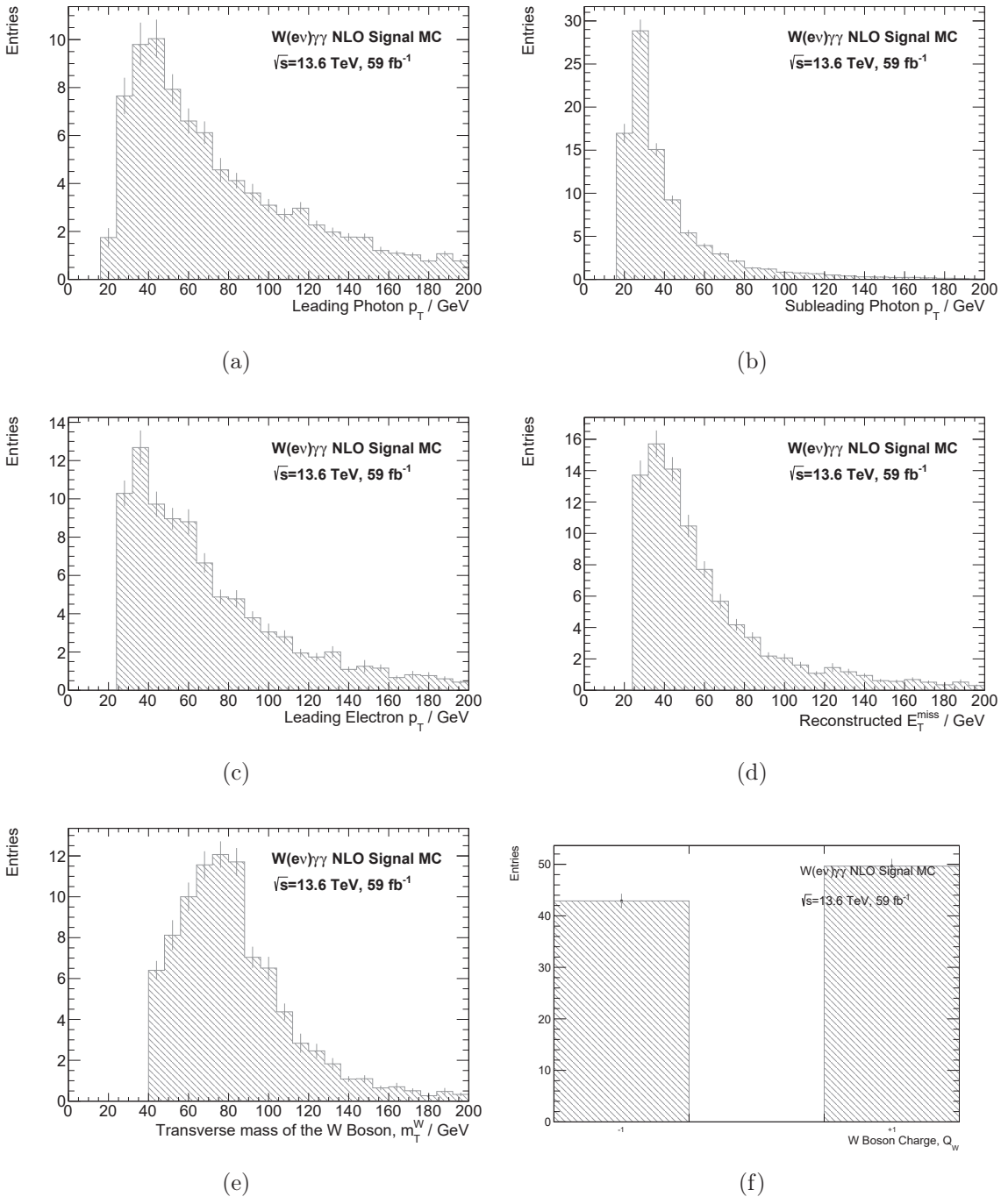

Figure 28: Final distributions of the leading and subleading photons, in (a) and (b); the leading electron in (c); the reconstructed missing transverse energy in (d); and the transverse mass and charge of the W boson in (e) and (f) respectively. All of them corresponding to the signal electron channel MC.

D Signal Muon Channel MC Results

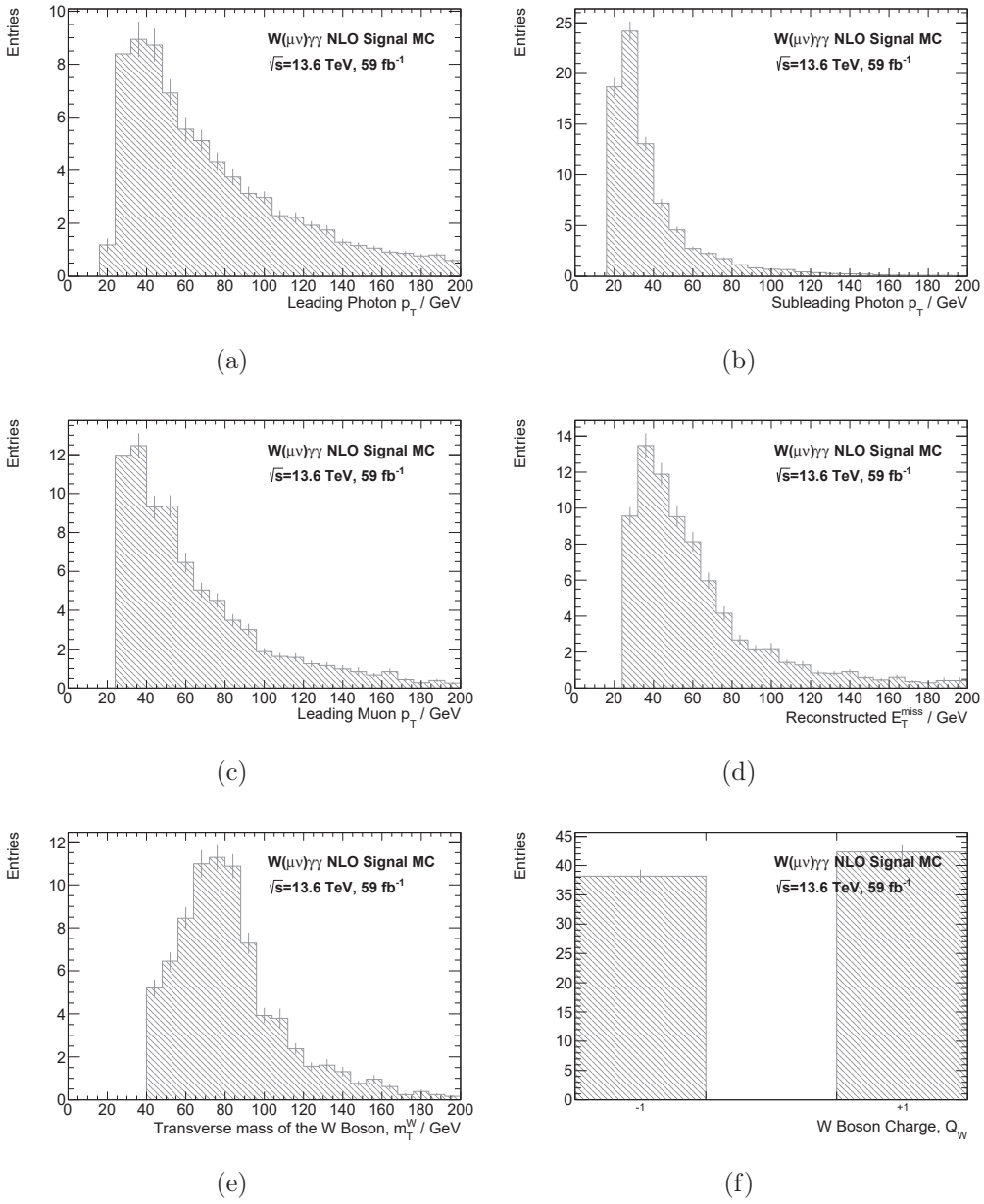

Figure 29: Final distributions of the leading and subleading photons, in (a) and (b); the leading electron in (c); the reconstructed missing transverse energy in (d); and the transverse mass and charge of the W boson in (e) and (f) respectively. All of them corresponding to the signal muon channel MC.

E Missing Transverse Energy Resolution

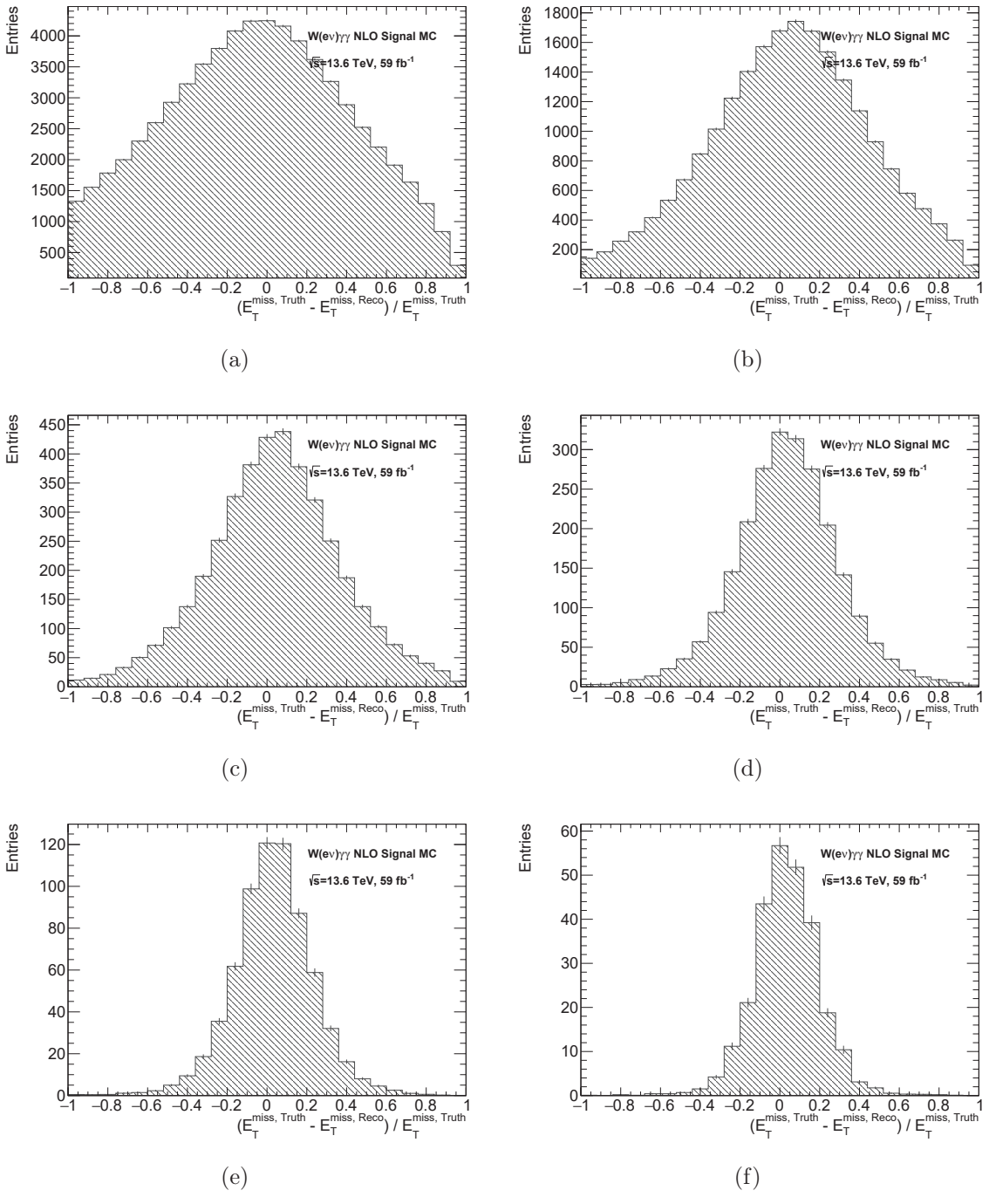

Figure 30: Missing Transverse resolution plots in bins of truth E_T^{miss}: (a) (20,40) GeV, (b) (40,60) GeV, (c) (60,80) GeV, (d) (80,120) GeV, (e) (120,160) GeV, (f) (160,200) GeV.

References

[1] Yiming Abulaiti. *Status of searches for dark matter at the LHC*. Tech. rep. Geneva: CERN, 2022. URL: https://cds.cern.ch/record/2799299.

[2] "Observation of $W\gamma\gamma$ triboson production in proton-proton collisions at $\sqrt{s} = 13$ TeV with the ATLAS detector". In: (2023). URL: http://cds.cern.ch/record/2853334.

[3] Mark Thomson. *Modern particle physics*. Cambridge University Press, 2013. ISBN: 9781107034266.

[4] *The Universe's building blocks*. URL: https://science.nasa.gov/universe/overview/building-blocks/l. (accessed: 19.03.2024).

[5] Anthony J.G.Hey Ian J.R. Aitchison. *Gauge Theories in Particle Physics*. CRC Press, 2013. ISBN: 978-1-4665-1299-3.

[6] X. Qian and P. Vogel. "Neutrino mass hierarchy". In: *Progress in Particle and Nuclear Physics* 83 (July 2015), pp. 1–30. ISSN: 0146-6410. DOI: 10.1016/j.ppnp.2015.05.002. URL: http://dx.doi.org/10.1016/j.ppnp.2015.05.002.

[7] Raul Jimenez et al. "Neutrino masses and mass hierarchy: evidence for the normal hierarchy". In: *Journal of Cosmology and Astroparticle Physics* 2022.09 (Sept. 2022), p. 006. ISSN: 1475-7516. DOI: 10.1088/1475-7516/2022/09/006. URL: http://dx.doi.org/10.1088/1475-7516/2022/09/006.

[8] Nicola Cabibbo. "Unitary Symmetry and Leptonic Decays". In: *Phys. Rev. Lett.* 10 (1963), pp. 531–533. DOI: 10.1103/PhysRevLett.10.531.

[9] Makoto Kobayashi and Toshihide Maskawa. "CP Violation in the Renormalizable Theory of Weak Interaction". In: *Prog. Theor. Phys.* 49 (1973), pp. 652–657. DOI: 10.1143/PTP.49.652.

[10] "Precision electroweak measurements on the Z resonance". In: *Physics Reports* 427.5 (2006), pp. 257–454. ISSN: 0370-1573. DOI: https://doi.org/10.1016/j.physrep.2005.12.006.

[11] Oscar Wallace Greenberg. "Color Charge Degree of Freedom in Particle Physics". In: *Compendium of Quantum Physics*. Ed. by Daniel Greenberger, Klaus Hentschel, and Friedel Weinert. Springer, 2009, pp. 109–111. ISBN: 978-3-540-70626-7. DOI: 10.1007/978-3-540-70626-7_32. URL: https://doi.org/10.1007/978-3-540-70626-7_32.

[12] The LHCb Collaboration. "Observation of $J/\psi p$ resonances consistent with pentaquark states in $\lambda^0 b \to J/\psi K^p$ decays". In: *Physical Review Letters* 115.7 (Aug. 2015). Ed. by J. C. Taylor. ISSN: 1079-7114. DOI: 10.1103/physrevlett.115.072001. URL: http://dx.doi.org/10.1103/PhysRevLett.115.072001.

[13] F. Englert and R. Brout. "Broken Symmetry and the Mass of Gauge Vector Mesons". In: *Phys. Rev. Lett.* 13 (1964). Ed. by J. C. Taylor, pp. 321–323. DOI: 10.1103/PhysRevLett.13.321.

[14] Peter W. Higgs. "Broken Symmetries and the Masses of Gauge Bosons". In: *Phys. Rev. Lett.* 13 (1964). Ed. by J. C. Taylor, pp. 508–509. DOI: 10.1103/PhysRevLett.13.508.

[15] The ATLAS Collaboration. "Observation of a new particle in the search for the Standard Model Higgs boson with the ATLAS detector at the LHC". In: *Physics Letters B* 716.1 (Sept. 2012), pp. 1–29. ISSN: 0370-2693. DOI: 10.1016/j.physletb.2012.08.020. URL: http://dx.doi.org/10.1016/j.physletb.2012.08.020.

[16] The CMS Collaboration. "Observation of a new boson at a mass of 125 GeV with the CMS experiment at the LHC". In: *Physics Letters B* 716.1 (Sept. 2012), pp. 30–61. ISSN: 0370-2693. DOI: 10.1016/j.physletb.2012.08.021. URL: http://dx.doi.org/10.1016/j.physletb.2012.08.021.

[17] M.D. Schwartz. *Quantum Field Theory and the Standard Model*. Quantum Field Theory and the Standard Model. Cambridge University Press, 2014. ISBN: 9781107034730. URL: https://books.google.de/books?id=HbdEAgAAQBAJ.

[18] Sheldon L. Glashow. "Partial-symmetries of weak interactions". In: *Nuclear Physics* 22.4 (1961), pp. 579–588. ISSN: 0029-5582. DOI: https://doi.org/10.1016/0029-5582(61)90469-2. URL: https://www.sciencedirect.com/science/article/pii/0029558261904692.

[19] A. Salam and J.C. Ward. "Electromagnetic and weak interactions". In: *Physics Letters* 13.2 (1964), pp. 168–171. ISSN: 0031-9163. DOI: https://doi.org/10.1016/0031-9163(64)90711-5. URL: https://www.sciencedirect.com/science/article/pii/0031916364907115.

[20] Steven Weinberg. "A Model of Leptons". In: *Phys. Rev. Lett.* 19 (21 Nov. 1967), pp. 1264–1266. DOI: 10.1103/PhysRevLett.19.1264. URL: https://link.aps.org/doi/10.1103/PhysRevLett.19.1264.

[21] Céline Degrande et al. "Effective field theory: A modern approach to anomalous couplings". In: *Annals of Physics* 335 (2013), pp. 21–32. ISSN: 0003-4916. DOI: https://doi.org/10.1016/j.aop.2013.04.016. URL: https://www.sciencedirect.com/science/article/pii/S0003491613000894.

[22] M. Aaboud et al. "Measurement of the production cross section of three isolated photons in pp collisions at $\sqrt{s} = 8\,\text{TeV}$ TeV using the ATLAS detector". In: *Physics Letters B* 781 (June 2018), pp. 55–76. ISSN: 0370-2693. DOI: 10.1016/j.physletb.2018.03.057. URL: http://dx.doi.org/10.1016/j.physletb.2018.03.057.

[23] M. Aaboud et al. "Study of $WW\gamma$ and $WZ\gamma$ production in pp collisions at $\sqrt{s} = 8\,8\text{TeV}$ and search for anomalous quartic gauge couplings with the ATLAS experiment". In: *The European Physical Journal C* 77.9 (Sept. 2017). ISSN: 1434-6052. DOI: 10.1140/epjc/s10052-017-5180-3. URL: http://dx.doi.org/10.1140/epjc/s10052-017-5180-3.

[24] G. et al. Aad. "Measurement of $Z\gamma\gamma$ production in pp collisions at $\sqrt{s} = 13\,\text{TeV}$ with the ATLAS detector". In: *The European Physical Journal C* 83.6 (June 2023). ISSN: 1434-6052. DOI: 10.1140/epjc/s10052-023-11579-8. URL: http://dx.doi.org/10.1140/epjc/s10052-023-11579-8.

[25] G. et al. Aad. "Observation of $WZ\gamma$ production in pp collisions at $\sqrt{s} = 13\,\text{TeV}$ with the ATLAS detector". In: *Phys. Rev. Lett.* 132.2 (2024), p. 021802. DOI: 10.1103/PhysRevLett.132.021802. arXiv: 2305.16994. URL: https://cds.cern.ch/record/2860061.

[26] G. et al. Aad. "Observation of WWW Production in pp collisons at $\sqrt{s} = 13\,\text{TeV}$ with the ATLAS Detector". In: *Physical Review Letters* 129.6 (Aug. 2022). ISSN: 1079-7114. DOI: 10.1103/physrevlett.129.061803. URL: http://dx.doi.org/10.1103/PhysRevLett.129.061803.

[27] G. et al. Aad. "Evidence for the production of three massive vector bosons with the ATLAS detector". In: *Physics Letters B* 798 (2019), p. 134913. ISSN: 0370-2693. DOI: https://doi.org/10.1016/j.physletb.2019.134913. URL: https://www.sciencedirect.com/science/article/pii/S0370269319306355.

[28] The ATLAS Collaboration. "Evidence of $W\gamma\gamma$ production in pp collisions at $\sqrt{s} =$ 8 TeV and limits on anomalous quartic gauge couplings with the ATLAS detector". In: *Physical Review Letters* 115.3 (July 2015). ISSN: 1079-7114. DOI: 10.1103/physrevlett.115.031802. URL: http://dx.doi.org/10.1103/PhysRevLett.115.031802.

[29] The CMS Collaboration. "Measurements of the pp → W and pp → Z cross sections and limits on anomalous quartic gauge couplings at $sqrts = 8\,\text{TeV}$". In: *Journal of High Energy Physics* 2017.10 (Oct. 2017). ISSN: 1029-8479. DOI: 10.1007/jhep10(2017)072. URL: http://dx.doi.org/10.1007/JHEP10(2017)072.

[30] The CMS Collaoration. "Measurements of the pp → W± and pp → Z cross sections at $\sqrt{s} = 13\,\text{TeV}$ and limits on anomalous quartic gauge couplings". In: *Journal of High Energy Physics* 2021.10 (Oct. 2021). ISSN: 1029-8479. DOI: 10.1007/jhep10(2021)174. URL: http://dx.doi.org/10.1007/JHEP10(2021)174.

[31] *The Large Hadron Collider*. URL: https://home.cern/science/accelerators/large-hadron-collider. (accessed: 19.03.2024).

[32] Oliver Sim Brüning et al. *LHC Design Report*. CERN Yellow Reports: Monographs. Geneva: CERN, 2004. DOI: 10.5170/CERN-2004-003-V-1. URL: https://cds.cern.ch/record/782076.

[33] *LHC the guide FAQ*. URL: https://home.cern/resources/brochure/knowledge-sharing/lhc-facts-and-figures. (accessed: 19.03.2024).

[34] Joao Pequenao. "Computer generated image of the whole ATLAS detector". 2008. URL: https://cds.cern.ch/record/1095924.

[35] The ATLAS Collaboration. "Jet energy scale and resolution measured in proton–proton collisions at $\sqrt{s} = 13$ TeV with the ATLAS detector". In: *Eur. Phys. J. C* 81.8 (2021), p. 689. DOI: 10.1140/epjc/s10052-021-09402-3. arXiv: 2007.02645. URL: https://cds.cern.ch/record/2722869.

[36] Mars Lyukova. *ATLAS LAr Calorimeter Commissioning for LHC Run-3*. Tech. rep. Geneva: CERN, 2024. URL: http://cds.cern.ch/record/2888545.

[37] The ATLAS Collaboration. *The ATLAS Trigger System for LHC Run 3 and Trigger performance in 2022*. Tech. rep. Geneva: CERN, 2024. arXiv: 2401.06630. URL: https://cds.cern.ch/record/2886407.

[38] ATLAS Collaboration. *The ATLAS Experiment at the CERN Large Hadron Collider: A Description of the Detector Configuration for Run 3*. 2023. arXiv: 2305.16623 [physics.ins-det].

[39] ATLAS Collaboration. *The ATLAS Trigger System for LHC Run 3 and Trigger performance in 2022*. Tech. rep. Geneva: CERN, 2024. arXiv: 2401.06630. URL: https://cds.cern.ch/record/2886407.

[40] ATLAS Collaboration. "The ATLAS inner detector trigger performance in pp collisions at 13 TeV during LHC Run 2". In: *The European Physical Journal C* 82.3 (Mar. 2022). ISSN: 1434-6052. DOI: 10.1140/epjc/s10052-021-09920-0. URL: http://dx.doi.org/10.1140/epjc/s10052-021-09920-0.

[41] The ATLAS Collaboration. "Topological cell clustering in the ATLAS calorimeters and its performance in LHC Run 1". In: *The European Physical Journal C* 77.7 (July 2017). ISSN: 1434-6052. DOI: 10.1140/epjc/s10052-017-5004-5. URL: http://dx.doi.org/10.1140/epjc/s10052-017-5004-5.

[42] W Lampl et al. *Calorimeter Clustering Algorithms: Description and Performance*. Tech. rep. Geneva: CERN, 2008. URL: https://cds.cern.ch/record/1099735.

[43] The ATLAS Collaboration. "Electron and photon performance measurements with the ATLAS detector using the 2015–2017 LHC proton-proton collision data". In: *Journal of Instrumentation* 14.12 (Dec. 2019), P12006–P12006. ISSN: 1748-0221. DOI: 10.1088/1748-0221/14/12/p12006. URL: http://dx.doi.org/10.1088/1748-0221/14/12/P12006.

[44] ATLAS Collaboration. "Electron and photon performance measurements with the ATLAS detector using the 2015–2017 LHC proton-proton collision data". In: *Journal of Instrumentation* 14.12 (Dec. 2019), P12006–P12006. ISSN: 1748-0221. DOI: 10.1088/1748-0221/14/12/p12006. URL: http://dx.doi.org/10.1088/1748-0221/14/12/P12006.

[45] ATLAS Collaboration. "Electron reconstruction and identification in the ATLAS experiment using the 2015 and 2016 LHC proton-proton collision data at $\sqrt{s} = 13$ TeV". In: *Eur. Phys. J. C* 79.8 (2019), p. 639. DOI: 10.1140/epjc/s10052-019-7140-6. arXiv: 1902.04655. URL: https://cds.cern.ch/record/2657964.

[46] Andres Eloy Pinto Pinoargote. *Results from muon reconstruction performance with ATLAS at Run-3*. Tech. rep. Geneva: CERN, 2023. URL: https://cds.cern.ch/record/2870384.

[47] ATLAS Collaboration. "Jet reconstruction and performance using particle flow with the ATLAS Detector". In: *The European Physical Journal C* 77.7 (July 2017). ISSN: 1434-6052. DOI: 10.1140/epjc/s10052-017-5031-2. URL: http://dx.doi.org/10.1140/epjc/s10052-017-5031-2.

[48] ATLAS Collaboration. "Muon reconstruction performance of the ATLAS detector in proton–proton collision data at $\sqrt{s}$=13 TeV". In: *The European Physical Journal C* 76.5 (May 2016). ISSN: 1434-6052. DOI: 10.1140/epjc/s10052-016-4120-y. URL: http://dx.doi.org/10.1140/epjc/s10052-016-4120-y.

[49] ATLAS Collaboration. *The performance of missing transverse momentum reconstruction and its significance with the ATLAS detector using 140 fb^{-1} of $\sqrt{s} = 13$ TeV pp collisions*. Tech. rep. Geneva: CERN, 2024. arXiv: 2402.05858. URL: https://cds.cern.ch/record/2888751.

[50] Andy Buckley et al. "General-purpose event generators for LHC physics". In: *Physics Reports* 504.5 (July 2011), pp. 145–233. ISSN: 0370-1573. DOI: 10.1016/j.physrep.2011.03.005. URL: http://dx.doi.org/10.1016/j.physrep.2011.03.005.

[51] S. Agostinelli et al. "GEANT4–a simulation toolkit". In: *Nucl. Instrum. Meth. A* 506 (2003), pp. 250–303. DOI: 10.1016/S0168-9002(03)01368-8.

[52] T. Gleisberg et al. *Monte Carlo models at the LHC*. 2004. arXiv: hep-ph/0407365 [hep-ph].

[53] T. Stelzer and W.F. Long. "Automatic generation of tree level helicity amplitudes". In: *Computer Physics Communications* 81.3 (July 1994), pp. 357–371. ISSN: 0010-4655. DOI: 10.1016/0010-4655(94)90084-1. URL: http://dx.doi.org/10.1016/0010-4655(94)90084-1.

[54] *ATLAS Athena Guide: Introduction*. URL: https://atlassoftwaredocs.web.cern.ch/athena/athena-intro/. (accessed: 25.03.2024).

[55] *Welcome to the Gaudi Project documentation*. URL: https://gaudi.web.cern.ch/gaudi/. (accessed: 25.03.2024).

[56] *DAODPhys*. URL: https://twiki.cern.ch/twiki/bin/view/AtlasProtected/DAODPhys. (accessed: 25.03.2024).

[57] Caterina Marcon et al. *Optimizing ATLAS data storage: the impact of compression algorithms on ATLAS physics analysis data formats*. Tech. rep. Geneva: CERN, 2023. URL: https://cds.cern.ch/record/2871990.

[58] Jana Schaarschmidt et al. *PHYSLITE - A new reduced common data format for ATLAS*. Tech. rep. Geneva: CERN, 2023. URL: https://cds.cern.ch/record/2870350.

[59] Ulla Blumenschein et al. *Measurement of the vector boson production cross sections and their ratios using the LHC Run 3 pp collision data at 13.6 TeV*. Tech. rep. Geneva: CERN, 2022. URL: https://cds.cern.ch/record/2841234.

[60] ATLAS Collaboration. *Measurement of ZZ production cross-sections in the four-lepton final state in pp collisions at $\sqrt{s} = 13.6$ TeV with the ATLAS experiment*. Tech. rep. Geneva: CERN, 2023. URL: https://cds.cern.ch/record/2873508.

[61] *Preliminary analysis of the luminosity calibration of the ATLAS 13.6 TeV data recorded in 2022*. Tech. rep. Geneva: CERN, 2023. URL: https://cds.cern.ch/record/2853525.

[62] *ATLAS Luminosity Calculator*. URL: https://atlas-lumicalc.cern.ch. (accessed: 10.04.2024).

[63] *Good Run Lists for Run 3 Analyses*. URL: https://twiki.cern.ch/twiki/bin/view/AtlasProtected/GoodRunListsForAnalysisRun3. (accessed: 10.04.2024).

[64] The ATLAS Collaboration. *The ATLAS Trigger System for LHC Run 3 and Trigger performance in 2022*. Tech. rep. Geneva: CERN, 2024. arXiv: 2401.06630. URL: https://cds.cern.ch/record/2886407.

[65] *ATLAS Isolation and Fake Forum*. URL: https://atlas-iff.docs.cern.ch/index.html. (accessed: 25.04.2024).

[66] Stefano Frixione. "Isolated photons in perturbative QCD". In: *Physics Letters B* 429.3–4 (June 1998), pp. 369–374. ISSN: 0370-2693. DOI: 10.1016/s0370-2693(98)00454-7. URL: http://dx.doi.org/10.1016/S0370-2693(98)00454-7.

[67] The ATLAS Collaboration. *Measurement of the W-boson mass and width with the ATLAS detector using proton–proton collisions at* $\sqrt{s} = 7$ *TeV*. Tech. rep. Geneva: CERN, 2023. URL: https://cds.cern.ch/record/2884691.

[68] R. L. Workman et al. "Review of Particle Physics". In: *PTEP* 2022 (2022), p. 083C01. DOI: 10.1093/ptep/ptac097.

Acknowledgements

The work presented here would not be near possible without all the support that I received during the last year.

First of all, I would like to thank my supervisor Prof. Dr. Hans-Christian Schultz-Coulon, who inspired me to join the ATLAS group at Heidelberg University for the Master Thesis. In the group, the unaccountable help and supportive environment that I received from everyone made me feel comfortable and pushed me to work harder every day.

Additional thanks go to Prof. Dr. Klaus Reygers, who kindly agreed to be the second corrector of the thesis.

I would also like to thank Dr. Rainer Stamen, whose supervision of my work and was essential for the discussion of new ideas. To Anke, Varsiha and Lisa, thank you for the warm environment in our shared office, as well as the discussions that helped me to improve significantly. Special thanks to Thomas, who guided me into the work from the very beginning and supported me unconditionally until the end of the thesis.

To all of my friends and housemates, thank you for enduring me during the most stressful moments and supporting me when I needed it the most.

Lastly, I would also like to thank my parents and grandmother for their understanding and unconditional support from the distance.